Investigation of the potentially multiferroic Swedenborgite Systems

A thesis submitted towards partial fulfilment of

BS-MS Dual Degree Programme

by

Shanu Dengre

Under the guidance of

Dr. Sunil Nair

Assistant Professor (IISER-Pune)

Indian Institute of Science Education and Research

Pune

Certificate

This is to certify that this thesis entitled ***Investigation of potentially multiferroic Swedenborgite Systems*** submitted towards the partial fulfilment of the BS-MS dual degree programme at the Indian Institute of Science Education and Research Pune represents original research carried out by ***Shanu Dengre*** at ***Indian Institute of Science Education and Research – Pune***, under the supervision of ***Dr. Sunil Nair*** during the academic year 2014 – 2015.

Shanu 25/3/15

Student

Name Shanu Dengre

25/MAR/15

Supervisor

Name Dr. Sunil Nair

Declaration

I hereby declare that the matter embodied in the report entitled " Investigation of potentially multiferroic Swedenborgite Systems" are the results of investigations carried out by me at the department of Physics, Indian Institute of Science Education and Research – Pune, under the supervision of Dr. Sunil Nair and the same has not been submitted elsewhere for any other degree.

Student Shanu 25/3/15

Name Shanu Dengre

Supervisor Sunil 25/MAR/15

Name Dr. Sunil Nair

Acknowledgement

- First of all, I sincerely thank my supervisor Dr. Sunil Nair (IISER-Pune), for giving me a great opportunity to work in his lab, for his continuous guidance and encouragement throughout this project, and most of all for his constant discussions and teachings without which this work would not have been possible.

- I would like to thank my senior lab mate Soumendra Nath Panja (PhD Student) for his wonder-full discussions and uninterrupted help throughout the project.

- I would like to than all the other labmates and friends of my lab starting with, Sarath kumar, Rohit Kumar, Avirup De, Charu Garg, Devika T D, Deepak John and Kaustav Dey for their constant "here and there" help, discussions and for making a wonder-full environment for working in the lab.

- I would like to thank Dr. Surjeet Singh and all the members of his lab, Koushik Karmakar, Rabindranath Bag, Vinayak Kulkarni, with a special thanks to Prachee Telang and Kshiti Mishra for letting me use their lab which not only just saved time but also allowed me to explore beyond my project.

- I would like to thank all my friends for dragging me away from my work and having an awesome time throughout my BS-MS life at IISER-Pune.

- I would like to thank Neelesh Dumbre, T.S. Yatish and Anil Shetty for helping me in utilizing the facilities at H-cross (Physics department IISER-Pune).

- At last, but not the least, I am greatly indebted and sincerely thank to my family for their constant and never ending support.

Abstract

Multiferroics are systems in which more than one ferroic order simultaneously coexists. In this project, we investigated some potentially multiferroic Swedenborgite systems with general formulae ABM_4O_7.For this purpose we synthesized a series of polycrystalline sample of swedenborgites $Dy_xCa_{(1-x)}BaCo_4O_7$ (x = 0 to 1) using solid state ceramic synthesis. Structural investigations of this series reveal that the as x changes from 0 to 1, the structure of the series changes from a less symmetric orthorhombic *Pbn21* to a more symmetric hexagonal *P63mc*. Magnetisation measurements (ZFC-FC and MH) shows that the two end members of the series $CaBaCo_4O_7$ and $DyBaCo_4O_7$ have a ferrimagnetic and a spin-glass ground states respectively. For the compounds with ($0.1 \leq x \leq 9$) the MH curves at 2K shows a non-saturating spin glass like behaviour. The high paramagnetic contribution of Dy^{3+} species mask transitions in the Co sublattice, but an attempt have been made to understand the magnetic properties of some systems by subtracting its paramagnetic contribution. Careful ac-susceptibility measurements would be required to clearly establish the magnetic phase diagram in this series of compounds.

Content

Chapter 1: Introduction

1.1) Multiferroics

1.1.1) Introduction to Multiferroics

The term multiferroics was first coined by *Hans Schmid* [1], and are systems in which more than 1 ferroic (Box 1) orders coexists within the same system. Magnetoelectric multiferroics are systems in which ferroelectric and (ferri, anti) ferromagnetic orders are present. In ferroelectric and ferromagnetic systems, spatial and time reversal symmetries (fig. 1.1) are broken respectively. Thus, in these Multiferroics, both spatial and time reversal symmetries are broken simultaneously. The fact that in these systems, ferroelectric (magnetic) order can be tuned using magnetic (electric) field make these systems technologically important, for example in the form of magnetoelectric sensors, 4-state logic etc [2][3].

Box 1: Glossary of terms

Ferroics

Ferroelectric - These are the systems with spontaneous electric polarisation **P** which is stable and switchable hysterically by an applied electric field **E**.

Ferromagnetic - These are the systems with spontaneous magnetization **M** which is stable and switchable hysterically by an applied magnetic field **H**.

Ferroelastic - These are the systems with spontaneous strain **ϵ** which is stable and switchable hysterically by an applied stress **σ**.

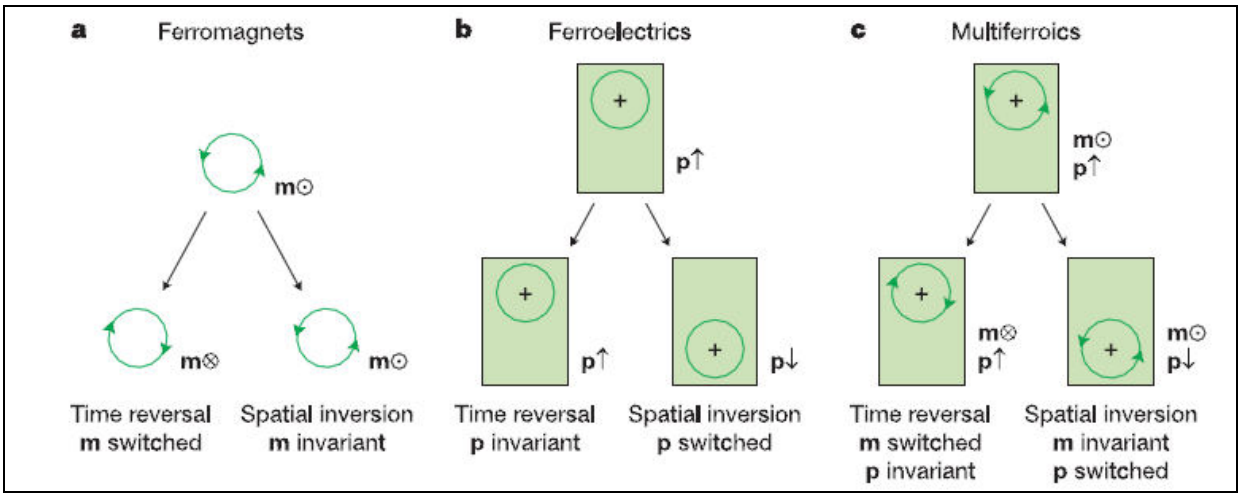

Fig. 1.1) Time-reversal and spatial-inversion symmetry in ferroics, a) ferromagnets, b) ferroelectric and c) multiferroics.[3]

1.1.2) The Magnetoelectric effect

In general, Magnetoelectricity refers to the coupling between electric and magnetic orders present in a material [4]. The free energy of a material in the presence of electric field and magnetic field is given by the relation –

$$F(E, H) = F_0 - P_i^S E_i - M_i^S H_i - \tfrac{1}{2}\varepsilon_0 \varepsilon_{ij} E_i E_j - \tfrac{1}{2}\mu_0 \mu_{ij} H_i H_j - \alpha_{ij} E_i H_j - \tfrac{1}{2}\beta_{ijk} E_i H_j H_k - \tfrac{1}{2}\gamma_{ijk} H_i E_j E_k \text{ -----} \quad (1.1)$$

Here, E and H are the electric and magnetic field respectively. On differentiating it, we will get Polarisation (P) as

$$P_i(E,H) = -\frac{\partial F}{\partial E_i} = P_i^S + \varepsilon_0 \varepsilon_{ij} E_j + \alpha_{ij} H_j + \tfrac{1}{2}\beta_{ijk} H_j H_k + \gamma_{ijk} H_i E_j \text{ ---------} \quad (1.2)$$

and magnetisation (M) as

$$M_i(E, H) = -\frac{\partial F}{\partial H_i} = M_i^S + \mu_0 \mu_{ij} H_j + \alpha_{ij} E_i + \beta_{ijk} E_i H_j + \tfrac{1}{2}\gamma_{ijk} E_j E_k \text{ --------} \quad (1.3)$$

Here, P^S and M^S are the spontaneous polarisation and magnetisation respectively, with ε and μ being the electric and magnetic susceptibilities. α_{ij} represents the coupling coefficient of the linear ME effect and β_{ijk} and γ_{ijk} are higher order coupling constants.

1.1.3) Types of Multiferroics

In all these multiferroics, the origin of magnetic order arises due to a partially filled *d* or *f*, shell, but the origin of ferroelectric order can vary from one system to another (fig. 1.2). Based on the origin of ferroelectric order, multiferroics are typically divided into 2 main classes [5]:

1.1.3.1) Type-1 Multiferroics

Type-1 Multiferroics have different origins for Ferromagnetic and Ferroelectric orders. Due to this, the coupling between these orderings is very low. In these multiferroics, the ordering of magnetic and ferroelectric orders typically occurs at 2 different temperatures, and generally the ferroelectric ordering temperature is higher than the magnetic ordering temperature. The magnitude of the observed electric polarisation **P** is of the order of 10-100 $\mu C\ cm^{-2}$. The mechanism for ferroelectric orders can also vary within the type-1 multiferroics, and some examples are as given below.

1.1.3.1.1) Ferroelectricity due to Off-Centre Shift

In the multiferroic perovskite $BaTiO_3$ [6], the body centred transition metal Ti^{4+} has a d^0 configuration. This empty d shell can be used to form a covalent bond with the surrounding

oxygen. The Ti^{4+} ion shifts from the centre of O_6 octahedra to form a strong covalent bond with 1 (or 3) oxygen ions at the expense of weakening the covalent bonds with other oxygens [7].

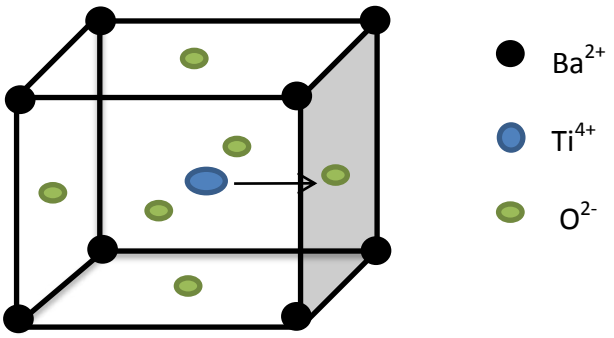

Fig. 1.2) represents the structure of $BaTiO_3$. The arrow represents the formation of strong covalent bond with a preferred oxygen atom in the O_6 octahedra.

1.1.3.1.2) Ferroelectricity due to the Lone Pair effect

In multiferroic $BiFeO_3$ [8], Bi^{3+} has 6*s* electrons which do not take part in the formation of bonds. These electrons are called *lone pairs* and they have high polarisability. The ferroelectric order in these compounds arises from the alignment of these lone pairs in a preferred direction [5, 7].

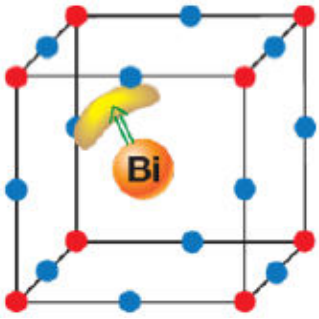

Fig. 1.3) represents the origin of ferroelectricity in $BiFeO_3$ [5].

1.1.3.1.3) Ferroelectrity due to Charge Ordering

Charge ordering can take place in any system due to bond ordering or site ordering. The spatial inversion symmetry of the system only breaks if both bond and site ordering are simultaneously present in the system (fig. 1.4). This will give rise the ferroelectric orders in the system. Multiferroicity, due to charge ordering is known to occur in the system $LuFe_2O_4$ [9].

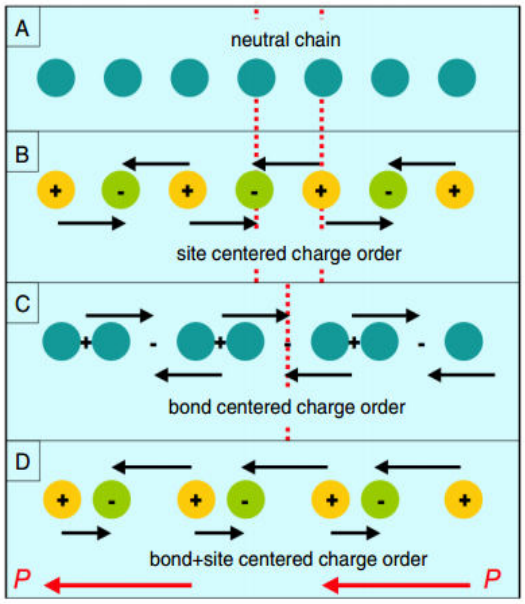

Fig. 1.4) represents the origin of ferroelectric order due to charge ordering. a) Neutral chain, b) site-centered charge ordering c) Bond centered charge ordering, d) Simultaneous presence of both bond and site charge ordering which breaks the spatial inversion symmetry making the structure non-centrosymmetric [10].

1.1.3.1.4) Ferroelectricity due to Geometry

In the multiferroic $YMnO_3$, the origin of ferroelectricity is due to the tilting of the whole bipyramidal MnO_5 polyhedra [11]. This gives rise to the formation of more than 1 type of Y-O bonds in $YMnO_3$. This breaks the spatial symmetry of the crystal and gives rise to ferroelectric polarisation in this system. [11]

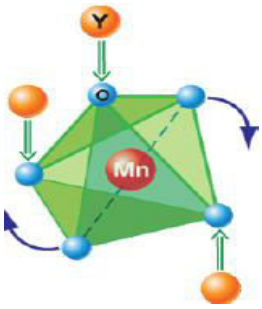

Fig. 1.5) represents the tilting of MnO5 polyhedra in $YMnO_3$ [5]

1.1.3.2) Type-2 Multiferroics

In Type-2 multiferroics, ferroelectric order arises due to a particular type of magnetic ordering. This allows them to have a large coupling between these orders. Also, in these multiferroics both magnetic and ferroelectric ordering occurs at the same temperature. This coupling makes type-2 multiferroics more technologically important, but a huge drawback of these multiferroics is that they typically have an induced **P** of the order of 10^{-2} μC cm^{-2}. The important question of how a magnetic ordering gives rise to the ferroelectricity in these multiferroics is now reasonably well established.

There are 2 main types of magnetic order responsible for breaking of inversion symmetry in the type-2 multiferroics. The first one is ferroelectricity due to spiral magnetic ordering like in the case of $TbMnO_3$ [12, 13], $Ni_3V_2O_8$ [14], $TbMn_2O_5$ [15], $Cu_3Nb_2O_8$ [16] and ferroelectricity due to collinear magnetic order as in case of Ca_3CoMnO_6 [17].

1.1.3.2.1 Ferroelectricity due to Spiral magnetic Ordering

In a spiral configuration, magnetic spins vectors lies on a plane such that their components on the 2 perpendicular axis on the plane have a periodic variation along an arbitrary direction [18]. Let S_i and S_j be two spins sitting at sites i and j. Let e_{ij} be a unit vector joining the sites i and j. A general expression relating the electric polarisation **P** and the spin rotation axis $S_i \times S_j$ is given by [19]

$$P \propto \Upsilon\, e_{ij} \times (S_i \times S_j) \qquad (1.4)$$

Here Υ is a constant which depends on the magnitude of the superexchange interaction and the spin orbit coupling [18, 19].
Based on the directions of e_{ij} and $S_i \times S_j$, these spiral configurations can be subdivided as sinusoidal, screw, cycloidal and conical (fig. 1.6). From the equation it is clear that there will be a finite polarisation if both the spin rotation axis $S_i \times S_j$ and the unit vector e_{ij} are finite and are not parallel to each other. This condition is satisfied in case of non-collinear cycloidal and conical spirals. In the multiferroics $TbMnO_3$ [12,13,19] and $Ni_3V_2O_8$ [14,19], the ferroelectric polarisation arises due to cycloidal magnetic ordering and in all these cases spatial inversion symmetry is broken due to spiral ordering.

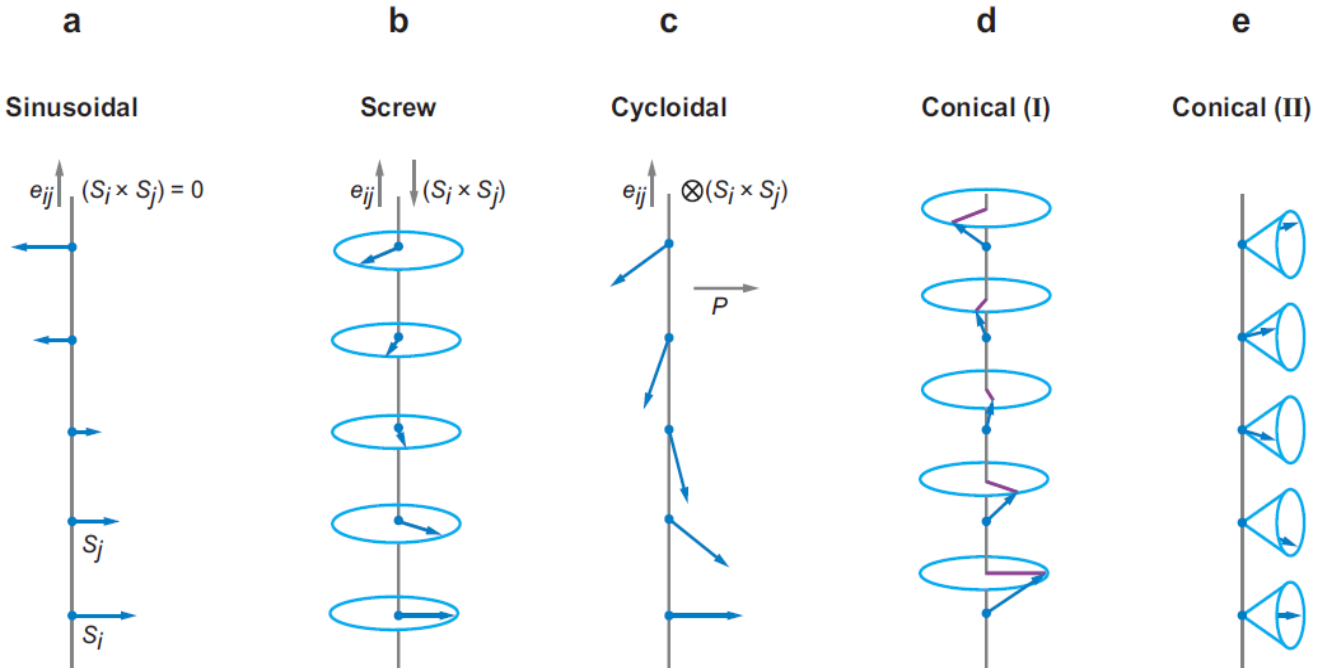

Fig. 1.6) represents the different forms of spiral magnetic ordering. a) Sinusoidal, b) Screw, c) cycloidal and d-e) Conical [18]

1.1.3.2.2) Ferroelectricity due to collinear magnetic orders

Collinear magnetic ordering refers to the alignment of magnetic moments along a particular axis. Ferroelectricity in these systems can be explained using a very simple model of frustrated chain with competing ferromagnetic (FM) and anti-ferromagnetic (AFM) interactions. In an Ising Chain in which the spins can either take *up* or *down* state with FM nearest neighbour interaction and AFM next nearest interaction, the magnetic ground state is made up of *up-up-down-down* (↑↑↓↓ arrangements of spins (fig. 1.7). The exchange striction between FM and AFM alignment causes shortening and stretching of bonds respectively. In a 1D chain of magnetic ions, in which magnetic ions say M1 and M2 are arranged alternatively (M1-M2-M1-M2) and M1 is positively charged with respect to M2 (+ - + -). This ordering together with the smaller and larger bond length due to FM and AFM interactions will lead to the breaking of inversion symmetry in this type of system resulting in the generation of ferroelectricity [20].

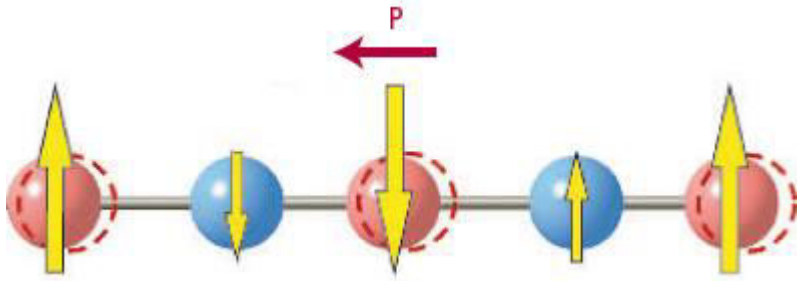

Fig. 1.7) shows the induced polarisation due to nearest neighbour FM and next nearest neighbour AFM interaction, Here both the (red and blue) species have different charge states.

This type of ferroelectricity is known to occur in the multiferroic Ca_3CoMnO_6 [17, 21]. It consists of the chains of Co^{2+} - Mn^{4+} - Co^{2+} - Mn^{4+} with (↑↑↓↓) spin configurations (fig. 1.8).

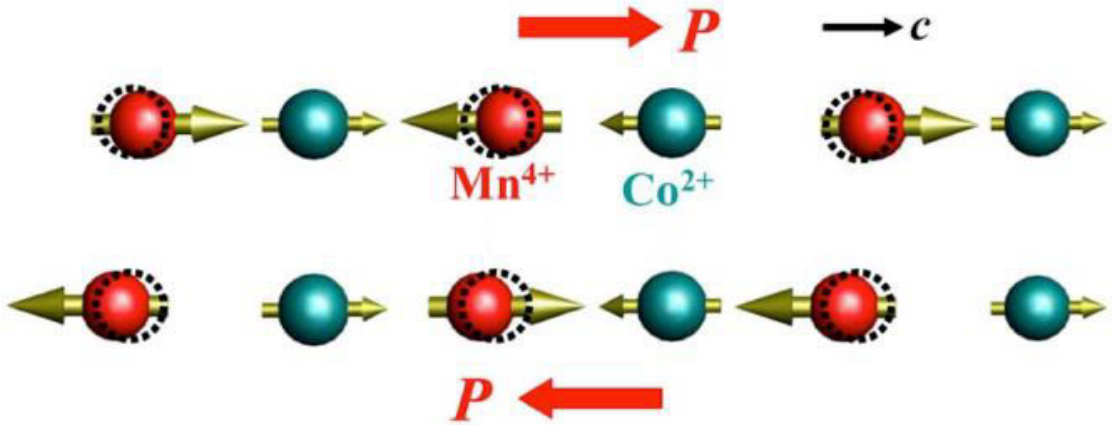

Fig. 1.8) indicates the induced polarisation due to the collinear magnetic arrangement of Co^{2+} and Mn^{4+} ions in Ca_3CoMnO_6 [17].

One of the current challenges for researchers is to design a room temperature multiferroic which has a polarisation magnitude as large as a Type-1 and a coupling as large as Type-2 multiferroic. In this project, we have investigated potentially multiferroic Swedenborgite systems. The following section on Swedenborgites focuses on answering the questions: What are Swedenborgites, why we should study them and what makes them potentially multiferroic?

1.2) Swedenborgites

1.2.1) History

Swedenborgite is a metal oxide mineral with chemical formulae $SbNaBe_4O_7$. It was discovered in the year 1924 in Sweden and named after a Swedish philosopher Emanual Swedenborg. It has a *P63mc* hexagonal symmetry. In this compound, the coordination number of Sb and Be is 6 (Octahedral) and 4 (Tetrahedral) respectively. The coordination number of Na varies from 6 to 12. $LuBaZn_3AlO_7$ is the first representative of a large family called as "114" oxides discovered by *Muller-Buschbaum et al.* [22]. This compound has the same structure as $SbNaBe_4O_7$.

In 2002, Martin Valldor and Magnus Andersson published their study of the structure and properties of single crystal and powdered $YBaCo_4O_7$ [23]. In 2004, Matin Valldor published his studies on disordered magnetism in the series $YBaCo_{4-x}Zn_xO_7$ (x = 0, 1, 2, 3) [24]. The attention of the scientific community grew towards Swedenborgites when Matin Valldor in 2004 successfully synthesised and analysed the structural properties of a series of compounds with formula $RBaX_4O_7$ (R = Ca, Y, In, Dy-Lu, X = Co, Al, Zn, Fe) [25]. The system becomes interesting, when magnetic ions like Fe and Co are substituted in place of Be. This allows the formation of alternate stacking of geometrically frustrated Kagome and Triangular layers in $RBaX_4O_7$. The following discussion explains the ground state degeneracy of triangular and kagome layers using Heisenberg and Ising spin models. The content of the next section 1.2.2 has been adopted from the Inaugral Dissertation of Stefan Buhrandt: University of Cologne [26].

1.2.2) Heisenberg and Ising spin models of triangular and kagome lattice

1.2.2.1) Triangular Lattice

A triangular lattice as shown in fig. 1.10a consists of edge sharing triangles. For the Heisenberg spin with antiferromagnetic nearest neighbour interaction in the lattice, the Hamiltonian (*H*) [26] is given by

$$H = J \sum_{i,j} S_i S_j \qquad (1.5)$$

Here <i,j> denotes the pair of nearest neighbours and J > 0 represents the antiferromagnetic interaction. The equation (1.5) can be written in the form as

$$H = (J/2) \sum_{\Delta} (S^1_{\Delta} + S^2_{\Delta} + S^3_{\Delta})^2 + \text{constant} \qquad (1.6)$$

Here S^1, S^2, S^3 represents 3 spins in the triangle Δ and the sum runs over all the triangles. From equation 1.6, it is clear that we will have a ground state if the sum of the spins in all triangles becomes zero.

$$S^1 + S^2 + S^3 = 0 \qquad (1.7)$$

This is possible if in all triangles the spins are arranged at 120° angles with respect to each other as shown in fig. 1.10b. If the spins are fixed in one of the triangle and because of the edge sharing the neighbouring triangles will share 2 spins and as per the equation 1.7 the neighbouring triangles will have a fixed arrangement of the spins. Following the same argument, there will only be a fixed arrangement of the spins throughout the lattice and thus the ground state will be unique.

a) b)

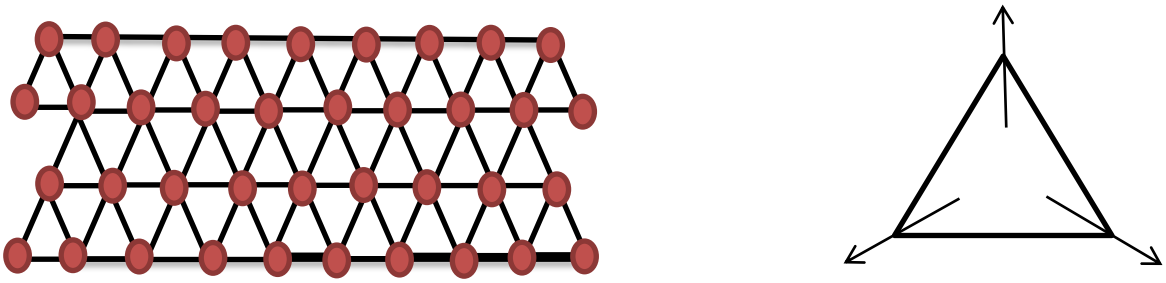

Fig. 1.10) (a) A typical Triangular lattice with edge sharing triangles b) Spin arrangements for the ground state of a triangle as per Heisenberg spins with antiferromagnetic next neighbour interaction (J > 0). All the spins equally share the frustration by aligning themselves at an angle of 120° with respect to each other [26].

If we consider the Ising spins (σ) in place of Heisenberg spins S, the *H* for this situation is given by

$$H = (J/2) \sum_{\Delta} (\sigma^1_{\Delta} + \sigma^2_{\Delta} + \sigma^3_{\Delta})^2 + \text{constant} \qquad (1.8)$$

In the Ising model all individual σ must be either + 1 or -1. As a consequence the sum of the spins in any triangle must be ± 1 (eq. 1.9).

$$\sigma^1_{\Delta} + \sigma^2_{\Delta} + \sigma^3_{\Delta} = \pm 1 \qquad (1.9)$$

After fixing the spins in one triangle in this configuration, the edge sharing neighbouring triangles can have more than one configuration after satisfying equation 1.9 one as shown in fig. 1.11. As a consequence of this, we will have a huge degeneracy in the ground state

which suppresses any specific ordering in the system. This system is an example of a spin glass.

Fig. 11) represents two different arrangements of the Ising spin in the neighbouring triangles of the triangular lattice. Both the arrangements satisfy the equation 1.9. Even after fixing the spin arrangement of upper triangle, the spin at lower triangle can arrange itself in 2 ways. [26]

1.2.2.2) Kagome lattice

We can get a kagome lattice as shown in fig. 1.12a [26] from a triangular lattice by removing one third of the lattice sites from it. Kagome lattice consists of corner sharing triangles rather than edge sharing in triangular lattice. This is an important factor while considering the ground state degeneracy of the kagome lattice.

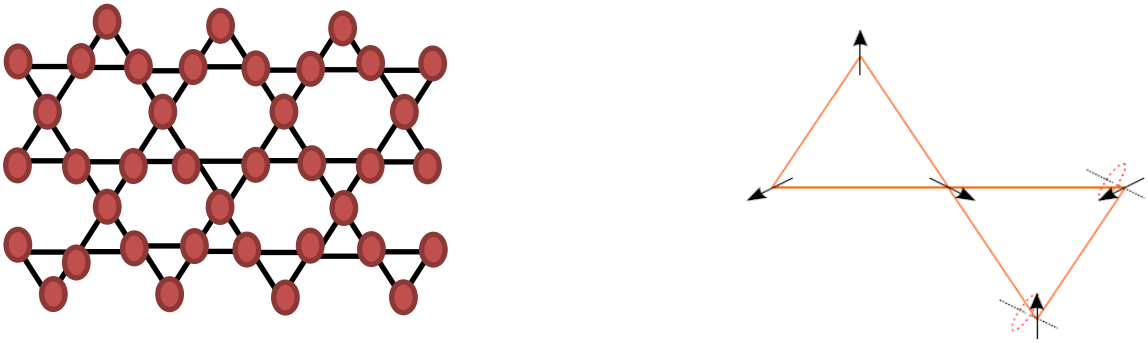

Fig. 1.12) (a) representation of kagome layer in 2D, (b) the degenerate ground states of a corner sharing neighbouring triangles of Kagome layer [26].

For the Heisenberg spins in kagome lattice, the ground state is calculated similar to the triangular case and will follow the equations 1.6 and 1.7. But the situation here is different because the neighbouring triangles share only one corner spin. If the spins in one triangle are fixed with 120° configuration, the other two non-mutual spins of the neighbouring triangle do not have a fixed configuration. These two spins can choose any configuration (fig. 1.12b) in the rotating axis defined by the corner sharing spin. This allows the spin-plane for the neighbouring triangle to be different, resulting in the macroscopic ground state degeneracy.

The similar analysis will be followed by the Ising spins in the kagome lattice. The system will only be constrained by the equations 1.8 and 1.9. The ground state degeneracy will be greater than the triangular case because the neighbouring triangles are less connected than the triangular lattice.
Stefan Buhrandt has studied the Swedenborgite lattice using both classical Heisenberg and antiferromagnetic Ising spins [27, 28]. Using Heisenberg model he showed the swedenborgites of the form RBaCo$_4$O$_7$ (R = rare earth) will display spin-liquid behaviour and entropic order by disorder phenomenon.

1.2.3) Structure and Properties of Swedenborgites

After the discovery of whole new series of compounds by Matin Valldor [25], the structure and properties of Swedenborgites have been the subject of extensive studies [29-62]. All these investigations confirm the exotic nature of Swdenborgites. Some interesting observations include the identification of a structural phase transition in REBaCo$_4$O$_7$ [38], the confirmation of a spin glass phase in YBaFe$_4$O$_7$ [36], and the observation of a ferrimagnetic ground state of CaBaCo$_4$O$_7$ [41-55]. Table 1.1 consists of the examples of Swedenborgites with their respective space group and symmetry at room temperature.

Table 1.1

Swedenborgite	Space group and symmetry
RBaCo$_4$O$_7$ (R = Ho, Dy, Er, Tm, Yb, Lu)	Hexgonal *P63mc* [25], or trigonal *P31c* [58]
CaBaCo$_4$O$_7$	Orthorhombhic *Pbn21* [41]
RBaFe$_4$O$_7$ (R = Dy, Ho, Er, Yb, Lu, Y)	Cubic *F-43m* [39]
RBaFe$_4$O$_7$ (R = Gd, Tb, Ca)	Hexgonal *P63mc* [39, 36]

In broad sense we can divide the structure of swedenborgites into 3 main categories - hexagonal *P63mc*, cubic *F-43m* and Orthorhombic *Pbn21*. All of these structures consists of tetrahedral framework of corner sharing "MO$_4$" (M = Co, Fe, Al, Zn etc) which gives rise to the formation of kagome and triangular layers. To understand the difference in the structure we will first start with the simplest hexagonal *P63mc* structures. The other two structures can be understood by simple modification of this structure. CaBaCo$_4$O$_7$ and DyBaCo$_4$O$_7$ are crucial components of this thesis and so in the last part of this section I have discussed the properties of CaBaCo$_4$O$_7$ and DyBaCo$_4$O$_7$.

1.2.3.1) Hexagonal P63mc structure

Apart from the arrangement of the CoO$_4$ tetrahedron as mentioned above, it consists of close packing of "O$_4$" and "BaO$_4$" layers forming a hexagonal "ABCB" close packed structure (fig. 1.13).

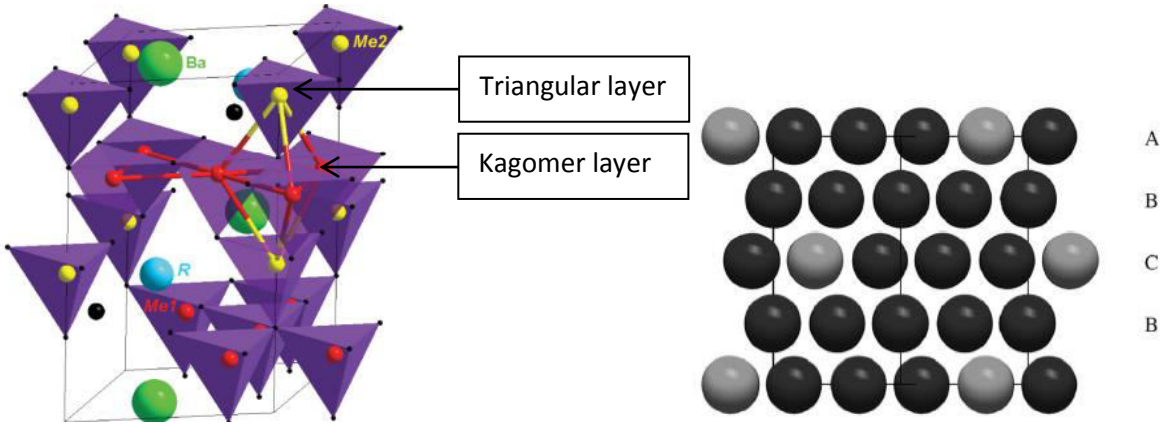

Fig. 13) (a) Structure of Hexgonal P63mc cobaltites $RBaCo_4O_7$ (R = Ho, Dy, Er, Tm, Yb, Lu), here Co1 and Co2 represents CoO_4 tetraheda forming kagome layer and triangular layers respectively [58], (b) Alternate Stacking of the "O_4" and "BaO_4" layer in "ABCB" fashion which leads to the formation of a hexagonal close packed structure [60].

1.2.3.2) Cubic Structure

Ferrites of the form $RBaFe_4O_7$ (R = Dy, Ho, Er, Yb, Lu, Y) shows cubic structure (fig. 1.14a). It consists of FeO_4 tetrahedral framework similar to the CoO_4 tetrahedral in $RBaCo_4O_7$ described above. In cubic ferrites, the stacking of "O_4" and "BaO_4" layers is in "ABC" (fig. 1.14b) fashion rather than "ABCB" as in the hexagonal case [39, 60].

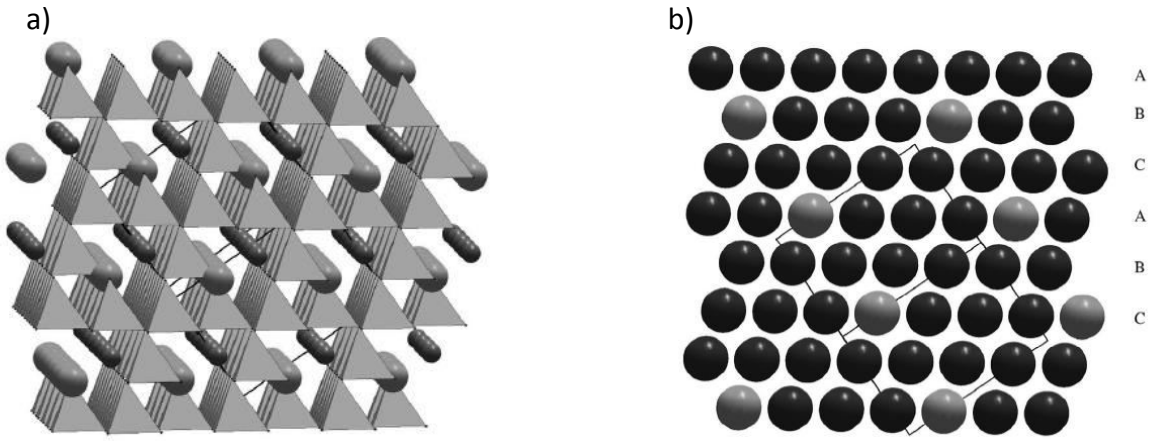

Fig. 1.14 a) shows the cubic structure of the ferrite $YBaFe_4O_7$ [60], b) stacking of "O_4" and "BaO_4" layers is in "ABC" fashion [60].

1.2.3.3) Orthorhombic Pbn21 structure

In the case of hexagonal *P63mc* structure, the plane of triangular and kagome layers remain parallel to each other. The structure of orthorhombic *Pbn21* differs from *P63mc* because of the strong buckling of the kagome layers. As a consequence, the M ions on kagome layers do not remain in one single plane. Also the kagome and triangular layers do not remain parallel. This leads to the formation of orthorhombic structure like in $CaBaCo_4O_7$ (fig. 1.15)

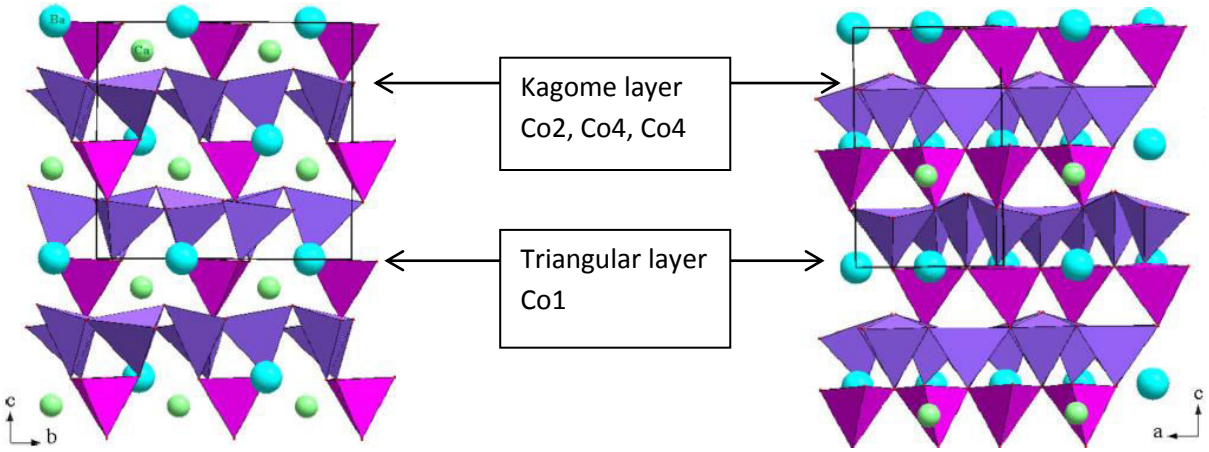

*Fig. 1.15) shows the structure of orthorhombic Pbn21 $CaBaCo_4O_7$ with the buckling of kagome layers along **a** and **b**-axis [42].*

1.2.4) $CaBaCo_4O_7$

1.2.4.1) what makes $CaBaCo_4O_7$ different from other "114" cobaltites of the form $RBaCo_4O_7$?

The crystal structure of $CaBaCo_4O_7$ is as described in previous section. The projection of the crystal structural of $CaBaCo_4O_7$ along ***a*** and ***b*** axis is shown in fig. 1.15 [42].The structure of $CaBaCo_4O_7$ is orthorhombic *Pbn21* in the whole temperature range of 4 – 300K [42], in contrast to the most of the $RBaCo_4O_7$ [40, 57, 61] as they generally show a structural transition from high temperature hexagonal (H) *P63mc* to low temperature orthorhombic (O) *Pbn21* symmetry. In this transition, cell parameters changes as $a_o \approx a_H \approx 6.3$ Å, $b_O \approx a_H\sqrt{3} \approx 11$ Å *and* $c_o \approx c_H \approx 10.2$ Å [42]. The distortion of hexagonal symmetry leads to the orthorhombic symmetry. This distortion (D) is quantified by the formulae-

$$D = ((b/\sqrt{3}) - a)/a \qquad (1.10)$$

Here a, b represents the lattice parameters of orthorhombic symmetry. An ideal hexagonal cell have D = 0, because $b = \sqrt{3}a$. The amplitude of D found in $CaBaCo_4O_7$ is largest among the "114" family [41, 42]. The x-ray and neutron diffraction studies of $CaBaCo_4O_7$ reveals that Co occupies 4 crystallographic sites (Co1, Co2, Co3 and Co4) in space group *Pbn21* and in contrast to the spin glass behaviour of geometrical frustrated $YBaCo_4O_7$ [23], it exhibits an ordered ferrimagnetic ground state [41, 42]. This different behaviour of $CaBaCo_4O_7$ from other "114" cobaltites is attributed to 3 reasons, (i) the buckling of Kagome layer lifts the geometrical frustration of the system, (ii) the Co shows charge ordering in 4 crystallographic sites [42] and (iii) The 1:1 ratio of Co^{3+}:Co^{2+}, which is 3:1 in case of RBaCo4O7 (R = RE, Y) [61].

1.2.4.2) Multiferroic behaviour of $CaBaCo_4O_7$

Out of 122 Shubinikov – Heesch point groups, there are 13 point groups which allow both spontaneous polarisation and magnetisation [1]. The ferrimagnetic state of $CaBaCo_4O_7$ has m'm2' symmetry [47], which belongs to one of these 13 point groups. In 2012, K. Singh *et al*

reported the multiferroic behaviour of $CaBaCo_4O_7$ [47]. They observed that dielectric measurements of ε' and tan δ shows a peak that coincides with the magnetic transition temperature T_c = 70K (fig. 1.17a and 1.17b). They measured a 16% change in the magneto-dielectric measurements at temperature 62 K under an applied field of 14 T (fig 1.17c). Dielectric measurements (fig. 1.17d) under different applied magnetic field confirmed the magnetic origin of polarisation. This work motivated a single crystal study of $CaBaCo_4O_7$ and in 2013, V. Caignaert *et al.* investigated the properties of a single crystalline specimen. The geometry of crystal allowed them to measure the **P** along the **c**-axis. In this geometry the formulae for P as per the equation 1.2 reduces to

$$\mathbf{P_c} = \alpha_{32}H_b + (\beta_{311}H_a^{\,2} + \beta_{322}H_b^{\,2} + \beta_{333}H_c^{\,2})/2 \qquad (1.11)$$

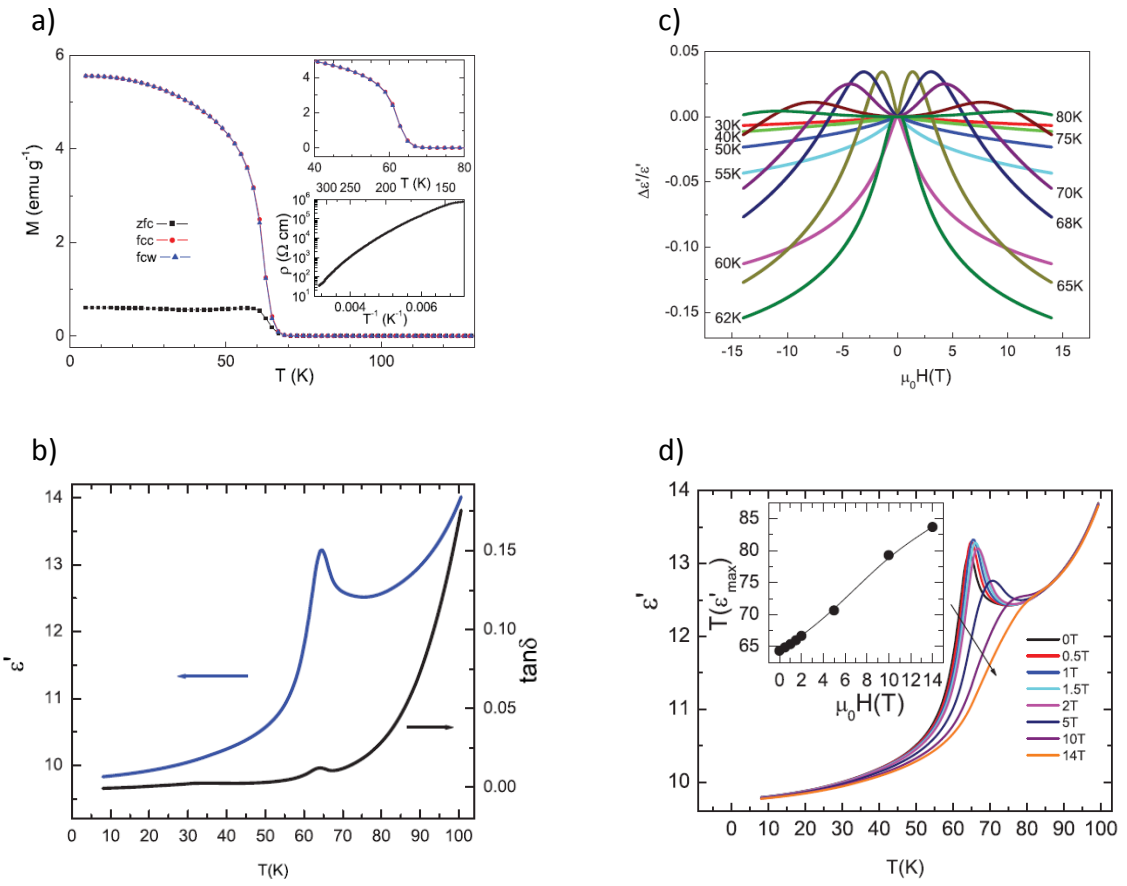

Fig. 1.17) (a) T dependence of M of $CaBaCo_4O_7$ with a T_c = 70 K, (b) T dependence of ε' and tan δ, showing that peaks of ε' and tan δ coincides with T_c, (c) the measure of magnetodielectric effect (Δ ε'/ ε', Δ ε' = Δ ε' (H) - Δ ε'(H=0)) as a function of magnetic field at different Temperatures, (d) T dependence of ε' as a function of H[47].

and since the magnetisation is measured along **b**-axis, the H is applied along the b-axis. Thus eq. further reduces to

$$\mathbf{P_c} = \alpha_{32}H_b + \beta_{322}H_b^{\,2}/2 \qquad (1.12)$$

Using this geometry they measured the magnetic field dependence of polarisation and observed the highest magnetically induced change in polarisation of $\Delta P = 17 mC/m^2$ [54] at 10 K.

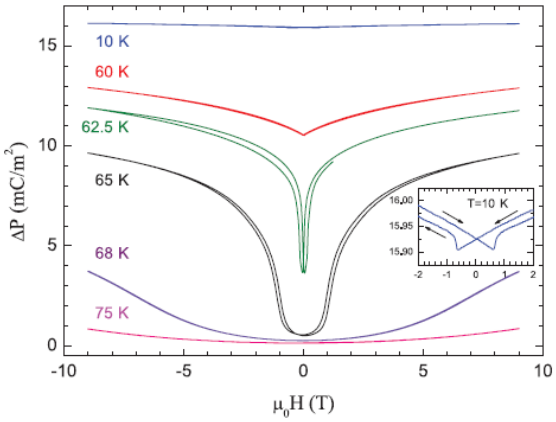

*Fig. 1.18) The Magnetic field dependence of change in electric polarisation (ΔP) at different temperatures. The measurements (ΔP) are done along the **c**-axis. Magnetic field is applied along **b**-axis [54].*

1.2.5) $DyBaCo_4O_7$

In earlier studies, $DyBaCo_4O_7$ has been reported to have a hexagonal *P63mc* symmetry [25]. In another report [56], the structure was also solved using space group *P31c* but for $DyBaCo_4O_7$ they did not get lower residuals than *P63mc*. The structure of $DyBaCo_4O_7$ is similar to the *P63mc* structure discussed in the section 1.2.3. In contrast to the structural transition shown by $RBaCo_4O_7$ (R = Ho, Er, Tm, Yb, and Lu), $DyBaCo_4O_7$ did not show any structural transition in the temperature range of 5 – 300K [38].

The magnetic and dielectric properties of $DyBaCo_4O_7$ are not fully explored. The expected behaviour of $DyBaCo_4O_7$ could be similar to the compounds like $RBaCo_4O_7$ and $RBaFe_4O_7$ for the rare earth R = Tb and Ho, which are close to Dy in the periodic table. The case of Fe is important if the magnetic properties are influenced by the charge ordering. In the single crystal study of done by R. Szymczak [62], they found that $TbBaCo_4O_7$ crystallises in space group *P63mc* and does not have a long range magnetic ordering down to 5K. They also found that a weak ferromagnetic ordering can be induced by the application of H ≈ 3T along c-axis (fig. 1.19).

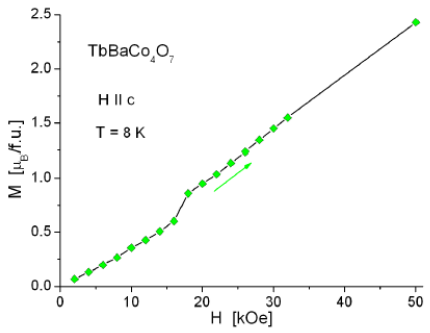

Fig 1.19) represents a weak ferromagnetic ordering along c-axis at H ≈ 3T [62] in $TbBaCo_4O_7$.

In contrast to the hexagonal *P63mc* space group of $TbBaCo_4O_7$, $HoBaFe_4O_7$ have a cubic structure and shows a show a spin glass behaviour with a $T_g \approx 50K$ (fig.1.20) [39].

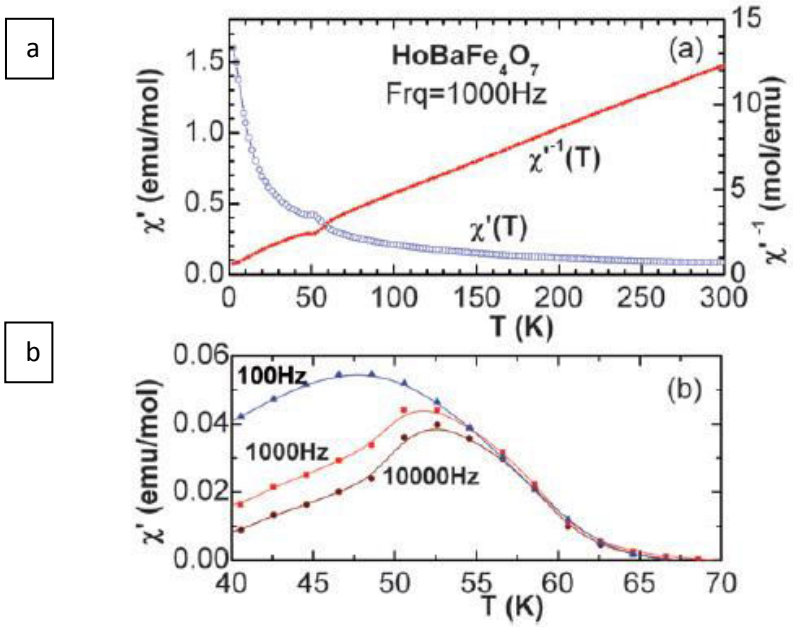

Fig. 1.20) (a) represents the χ' vs T measurements for $HoBaFe_4O_7$, (b) represents the dependence of χ' at frequencies of 100Hz, 1KHz and 100KHz after the subtraction of the paramagnetic contribution of Ho^{3+} [59].

1.1.4) Plan of the thesis and motivation for present work

The aim of present work is motivated by the fact that Swedenborgites are geometrical frustrated systems and that they also stabilise in the non-centrosymmetric space groups like *Pbn21, P63mc* and *P31c*, which makes them suitable candidates for the existence of multiferroicity. Also the structural and properties of swedenborgites ($RBaCo_4O_7$) hugely depends upon the average charge states of Co ions. In this project I have investigated polycrystalline samples of $Dy_xCa_{(1-x)}BaCo_4O_7$ series. In this series the average charge state of Co varies from +2.5 to +2.25 as x changes from 0 to 1. The aim of this project is to investigate the structural and magnetic/dielectric properties of these potentially multiferroic Swedenborgite systems.

Chapter 2: Methods

2.1 Sample Preparation

All the polycrystalline samples described in this report were synthesised using Solid State Synthesis method [63]. Stoichiometric amounts of high purity oxides and carbonates were thoroughly mixed using mortar and pestle. Typically 2-3 heat treatments varying from 24-48 hours in the temperature range of 900°C to 1100°C with intermediate grindings were given. All the samples were pelletised before the final treatments and also quenched down to room temperature. The details of the heat treatments for the synthesis of series $Dy_xCa_{(1-x)}BaCo_4O_7$ is given in the table 2.1.

Table 2.1

Sno.	Name of the Compounds	Treatment 1	Treatment 2	Treatment 3
1	$Dy_xCa_{(1-x)}BaCo_4O_7$: x = 0 to 0.5 for Δx = 0.1	900°C	1000°C	1050°C
2	$Dy_xCa_{(1-x)}BaCo_4O_7$: x = 0.5 to 1 for Δx = 0.1	900°C	1000°C	1100°C

2.2 Structural analysis of the X-Ray Diffraction data

In this project, X-Ray diffraction (XRD) patterns for all the samples ($Dy_xCa_{(1-x)}BaCo_4O_7$) were measured using a CuKα radiation (λ ≈ 1.540600Å). Patterns were calculated for range of 2θ from 10° to 80°. The step size for each measurement was 0.01°. The peaks in the XRD pattern represent different planes defined by Miller indices (h, k, l) values of the planes. The analysis of powder diffraction data is done by using Reitveld method [64]. This method is based upon the minimisation of a quantity called residual S_y using least square method [64]. S_y is defined as:

$$S_y = \sum_i w_i(y_i - y_{ci})^2 \qquad (2.1)$$

here, $w_i = 1/y_i$,

y_i = observed intensity at i^{th} step,

y_{ci} = calculated intensity at i^{th} step, and

$\sum$ runs over all the data points.

The calculated intensity (y_{ci}) is calculated using the formulae [64]:

$$y_{ci} = s \sum L_k |F_k|^2 Ø(2\theta_i - 2\theta_k) P_k A + y_{bi} \qquad (2.2)$$

here, s is the scale factor,

K represents the Miller indices (h, k, l) for a Bragg reflection,

L_k contains the Lorentz, Polarisation and the multiplicity factor,

Ø represents the reflection profile function,

P_k is the preferred orientation,

A is the absorption factor,
F_k is the structure factor for the k^{th} Bragg reflection and
y_{bi} is the background intensity at the i^{th} step.

To understand whether the fit has reached true global or false minima, various mathematical criteria are defined called as R-values. Some of the most commonly used R-values are

R-structure factor (R_F) = $$\frac{\sum|(I_k(obs))^{1/2} - (I_k(cal))^{1/2}|}{\sum(I_k(obs))^{1/2}} \quad (2.3)$$

R-Bragg factor (R_B) = $$\frac{\sum|I_k(obs) - I_k(cal)|}{\sum I_k(obs)} \quad (2.4)$$

R-Pattern (R_P) = $$\frac{\sum|y_i(obs) - y_i(cal)|}{\sum y_i(obs)} \quad (2.5)$$

R-weighted patten (R_{WP}) = $$\left\{\frac{\sum w_i(y_i(obs) - y_i(cal))^2}{\sum w_i(y_i(obs)^2}\right\}^2 \quad (2.6)$$

R-expected (R_E) = $$[(N-P)/\sum w_i y_{oi}]^{1/2} \quad (2.7)$$

Here, I_k represents the intensity calculated after the refinement cycle at the k^{th} Bragg reflection, N and P represents number of observations and parameters refined respectively. The goodness of fit indicator S is

$$S = S_y/(N-P)^{1/2} = R_{WP}/R_E \quad (2.8)$$

A satisfactory fit should have an S value equal to or less than 1.3 [64]. Reitveld refinement is a powerfull technique because it is able to distinguish between overlapping of the peaks in the powder X-ray and neutron diffraction patterns. But one needs to have a reasonably good starting model to avoid the convergence of the profile into false minima. In this project Fullprof software is used for Rietveld analysis [65].

2.3 Magnetisation measurements

Bulk magnetisation measurements were performed using an Quantum Design Magnetic Properties Measurement System (MPMS) XL magnetometer [66]. A non-magnetic capsule and straw are used as sample holder (fig. 2.1a). First the capsule filled with small (2-80mg) amount of powdered sample and it is placed inside the straw. Kapton tape is used to hold the sample tightly. This holder is attached to sample rod and inserted into the sample chamber such that the sample lies in within the region of measurement of the superconducting pick-up coils (fig. 2.1b).

A magnetic field is applied such that pick-up coil can detect the induced magnetic moment of the sample. Based on the sample position (z), SQUID generates a Voltage response. It is utilised for the centring of the sample such that all 4 pick-up coils sense the magnetic moments of the sample [67]. The movement of the sample produces a current proportional to the magnetic moment of the sample in the superconducting pickup coils. The change in currents produces magnetic field near SQUID which acts as a magnetic flux to voltage converter and produces a voltage signal corresponding to the magnetic movement of the sample.

In this project, DC magnetisation measurements were used to measure the Zero Field Cooled (ZFC) and Field Cooled (FC) modes. In ZFC and FC modes, samples were cooled down to 2K without and with a measuring field respectively. Measurements were performed during warming from 2 – 300K in both the modes. Isothermal magnetisation measurements were performed for all the samples at 2 and 300 K for an applied field of range -7T to 7T.

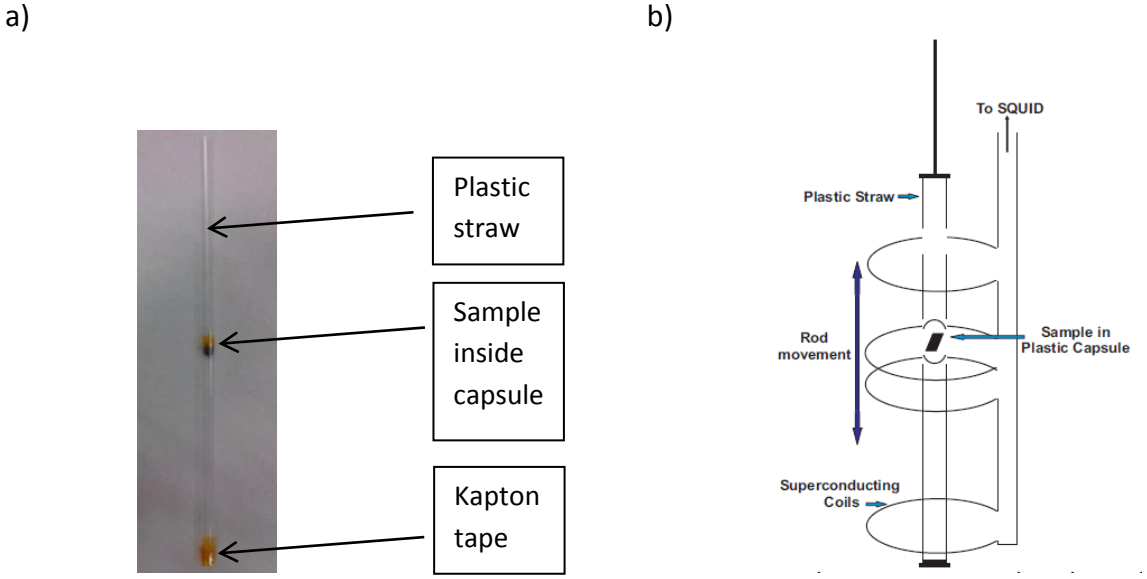

Fig. 2.2) (a) sample holder made up of plastic straw and capsule, (b) A vertical view of the sample holder and its position relative to the 4 superconducting coils [68].

2.4 Dielectric Measurements

A dielectric material can be electrically polarised by placing it in an electric field. For a parallel plate geometry, dielectric constant (ε_r) of the material is related to its capacitance (C) as-

$$C = \frac{\varepsilon_r \varepsilon_0 A}{d} \qquad (2.9)$$

here, A and d are the surface area and thickness of the sample respectively, ε_0 represents

the electrical permittivity of the free space (8.85 x 10^{-12} Fm^{-1}). For a sample with known dimensions, we can measure the dielectric constant (ε_r) by measuring the capacitance of the material using the above equation.
In this project all the dielectric measurements were performed in a closed cycle refrigerator (CCR), in the temperatures range of 15K - 300 K. The capacitance of the sample is measured by using a Novacontrol Alpha A frequency analyser. This analyser has operating frequency range of 3 µHz to 20 MHz and an impedance range – 0.01 to 10^{14} Ω. A sample holder made up of copper in which a thin (thickness < 1.5mm) cylindrical shaped and flat surface pellet of the sample is inserted. The sample is sandwiched in between the + and – electrodes of the sample holder (fig. 2.3a) and the impedance (Z) of the sample is measured using the frequency analyser.

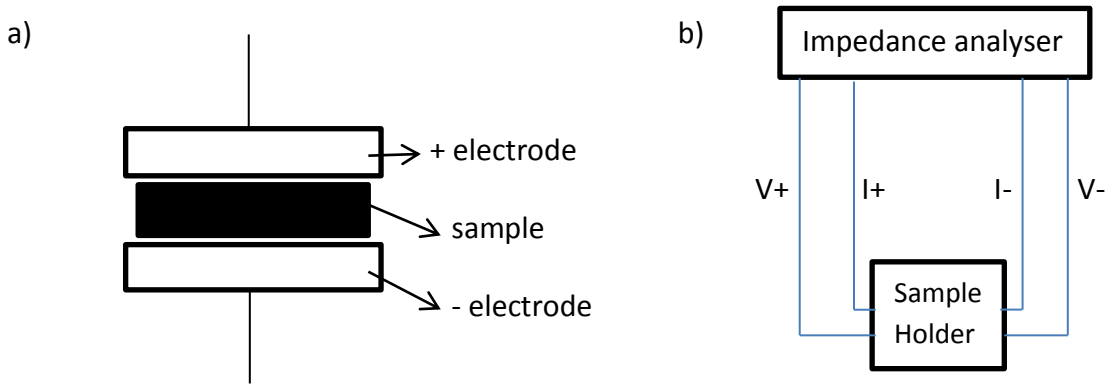

Fig. 2.3) (a) represents the parallal plat geometry and (b) represents a circuit diagram of the setup.

In this project dielectric constant (ε') and dielectric loss (tanδ) are measured as a function of temperature which ranges from 15K to 280K with a sweeping rate of 0.5-3K. First the sample is cooled down to the minimum possible temperature (≈ 15K) and measurements are done during warming. Depending upon the signal strength of the sample, measurements were performed for frequencies 1 KHz, 10 KHz or 100 KHz.

Chapter 3: Results and Analysis

3.1) X-Ray powder diffraction and Rietveld Refinements

3.1.1) $CaBaCo_4O_7$ and $DyBaCo_4O_7$

The XRD patterns of $CaBaCo_4O_7$ and $DyBaCo_4O_7$, shows that both these samples have single phase, and no impurity peaks were observed. Rietveld Refinement of the XRD data (fig 3.1) confirms the formation of $CaBaCo_4O_7$ in the orthorhombic *Pbn21* symmetry with lattice constants a = 6.2776(1) Å, b = 10.9900(8) Å and c = 10.1754(6) Å. The $DyBaCo_4O_7$ specimen is seen to crystallise in the hexagonal *P63mc* symmetry with lattice constants a = 6.3115(2) Å, b = 6.3115(2) Å and c = 10.2412(7) Å. The goodness of fit S values as determined from Rietveld Refinement for $CaBaCo_4O_7$ and $DyBaCo_4O_7$ are 1.24 and 1.35 respectively. All these results are in good agreement with the previous reports [41], [42], [44],[25].

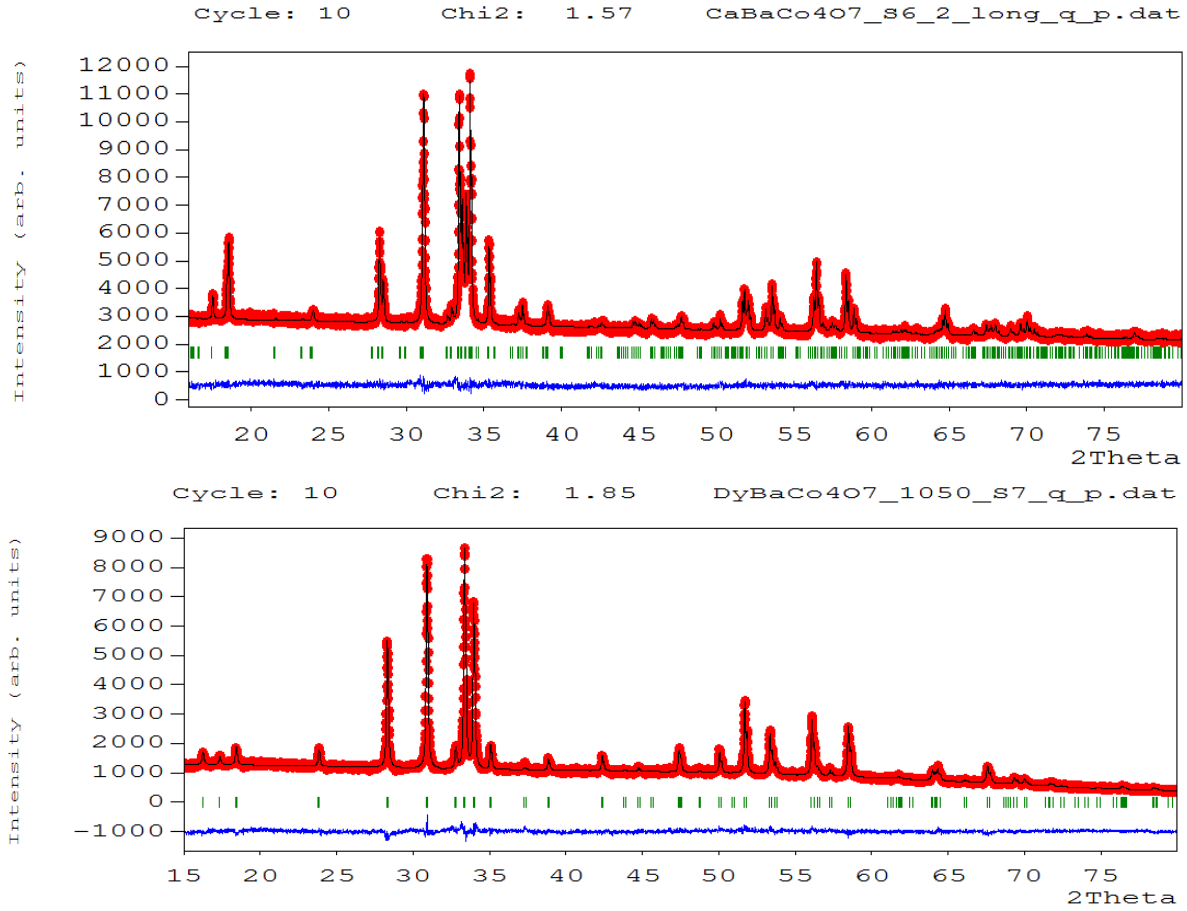

Fig 3.1) (a) and (b) represents Rietveld analysis of the XRD data of $CaBaCo_4O_7$ and $DyBaCo_4O_7$ respectively. Red and Black lines represent the experimental and calculated patterns respectively. The Blue line represents the difference between the two patterns.

3.1.2) The series $Dy_xCa_{(1-x)}BaCo_4O_7$

The two end members ($CaBaCo_4O_7$ and $DyBaCo_4O_7$) of the series have space groups *Pbn21* and *P63mc* respectively. Section 1.2.3 explains both of these structures in detail. From the Rietveld Refinement we find that the number of observed Braggs peak for the 2θ range of 15° – 80° are 230 and 56 for the space groups *Pbn21* and *P63mc* respectively. Moreover a clear distinction between these 2 space groups can be made by observing the XRD patterns in the 2θ range between 33° – 34.5°. The numbers of Bragg reflections in this region are greater for space group *Pbn21* than *P63mc*. This is shown in fig 3.2 (a) and (b)

a) *Pbn21* - $CaBaCo_4O_7$ b) *P63mc* - $DyBaCo_4O_7$

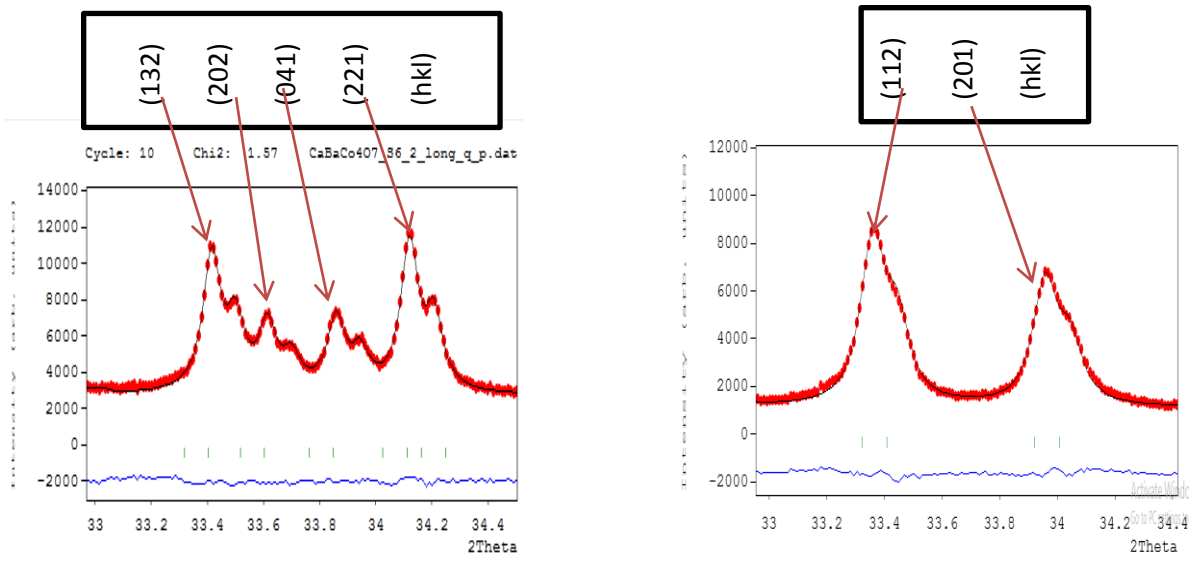

Fig 3.2) which shows the expanded region of Rietveld Refinement in between 33° – 36° for the $CaBaCo_4O_7$ and $DyBaCo_4O_7$ specimens respectively.

No impurity peak was observed in the XRD patterns of all the compounds ($Dy_xCa_{(1-x)}BaCo_4O_7$) (fig 3.3) and by observing the intensity patterns in the 2θ range of 33° – 34.5°, As x changes from 0 to 1 the number of observed Braggs reflection decreases, which also supports the fact that for this series as x increases, the space group changes from a less symmetric orthorhombic *Pbn21* to more symmetric hexagonal *P63mc*. Utilising this information about space groups of the series $Dy_xCa_{(1-x)}BaCo_4O_7$ we are in the process of performing the Rietveld Refinement of the whole series. A few representative graphs are shown in fig 3.5, and their results are tabulated in table 3.1. Fig. 3.6 represents the variation of lattice parameters as a function of x for samples having hexagonal *P63mc* space group (x = 0.6 to 1).

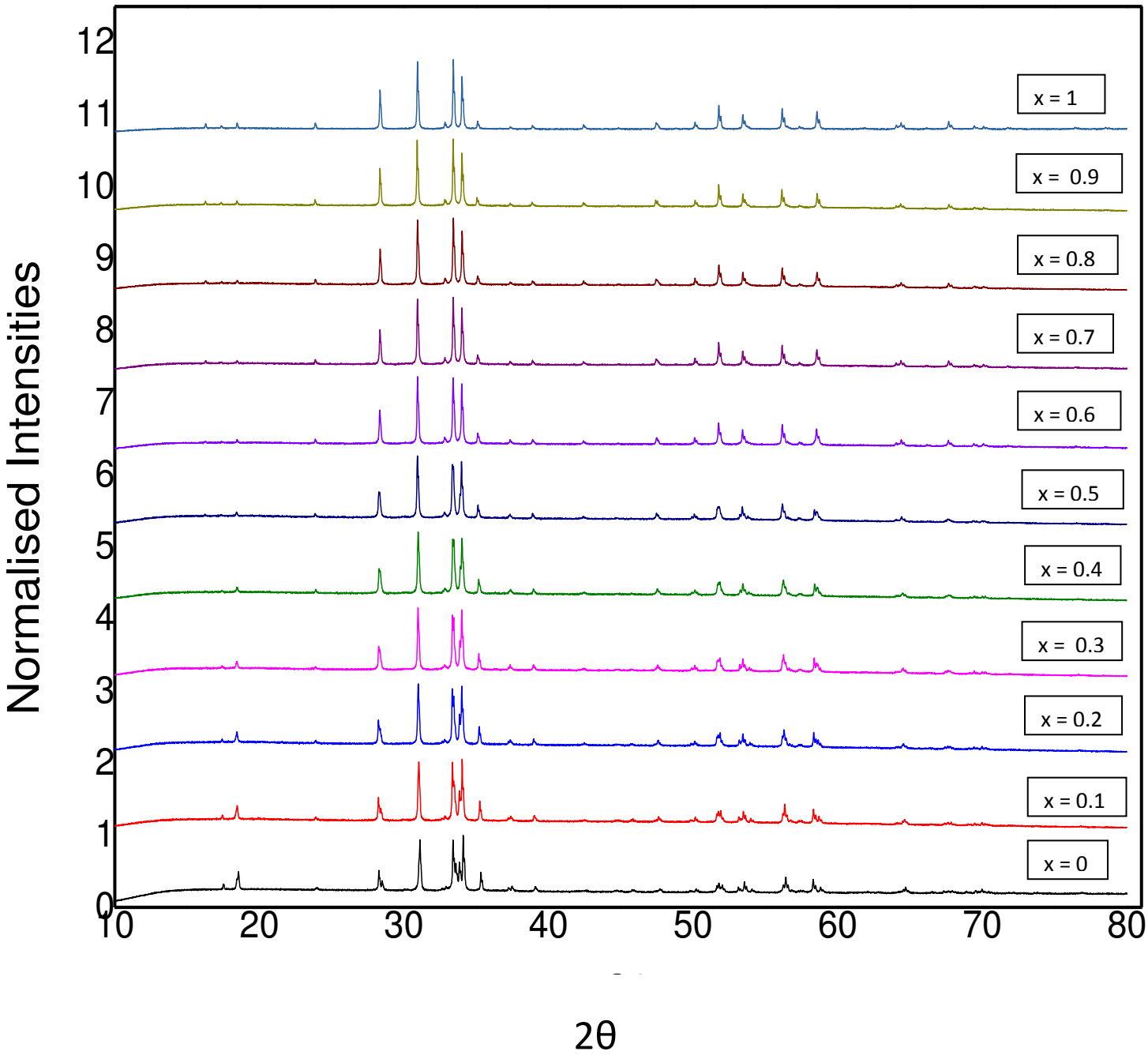

Fig 3.3) XRD patterns for the series $Dy_xCa_{(1-x)}BaCo_4O_7$. All the 11 patterns in between represents $Dy_xCa_{(1-x)}BaCo_4O_7$ with x = 0 to 1 with Δx = 0.1 from bottom to top respectively. The bottom most pattern (black) is for $CaBaCo_4O_7$ with x = 0 and the topmost pattern (light blue) is for $DyBaCo_4O_7$ with x = 1.

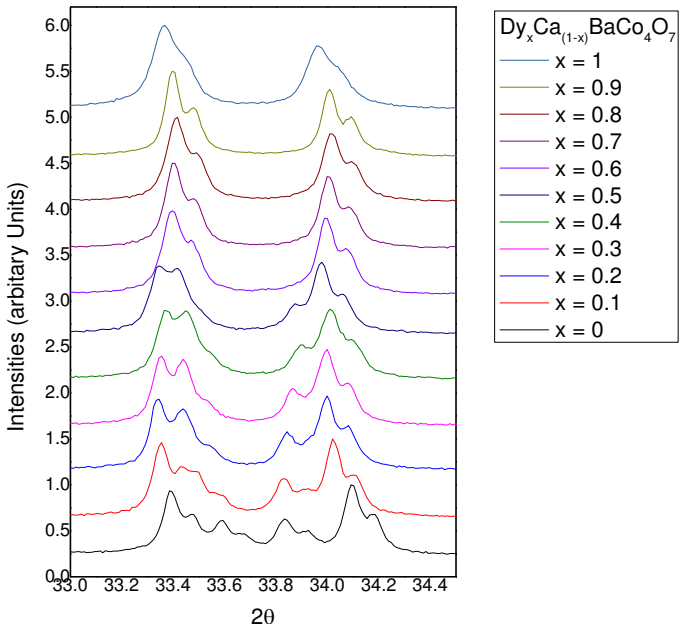

Fig. 3.4) shows the XRD patterns for the series DyxCa$_{(1-x)}$BaCo$_4$O$_7$ for the 2θ range of 33° – 34.5°. The intensity patterns are similar for x in between 0 to 0.5 and these compounds have space group orthorhombic Pbn21. The intensity patterns for the compounds with 0.6 ≤ x ≤ 1 are similar and have hexagonal space group P63mc.

Table 3.1

Sample name	Space group	a(Å)	b(Å)	c(Å)	S =R_{wp}/R_e
$DyBaCo_4O_7$	*P63mc*	6.3115(2)	6.3115(2)	10.2412(7)	1.35
$Dy_{0.9}Ca_{0.1}BaCo_4O_7$	*P63mc*	6.3068(5)	6.3068(5)	10.2492(9)	1.36
$Dy_{0.8}Ca_{0.2}BaCo_4O_7$	*P63mc*	6.3102(6)	6.3102(6)	10.2453(9)	1.44
$Dy_{0.7}Ca_{0.3}BaCo_4O_7$	*P63mc*	6.3103(3)	6.3103(3)	10.2434(5)	1.34
$Dy_{0.6}Ca_{0.4}BaCo_4O_7$	*P63mc*	6.3120(2)	6.3120(2)	10.2383(9)	1.34
$CaBaCo_4O_7$	*Pbn21*	6.2776(1)	10.9900(8)	10.1754(6)	1.24

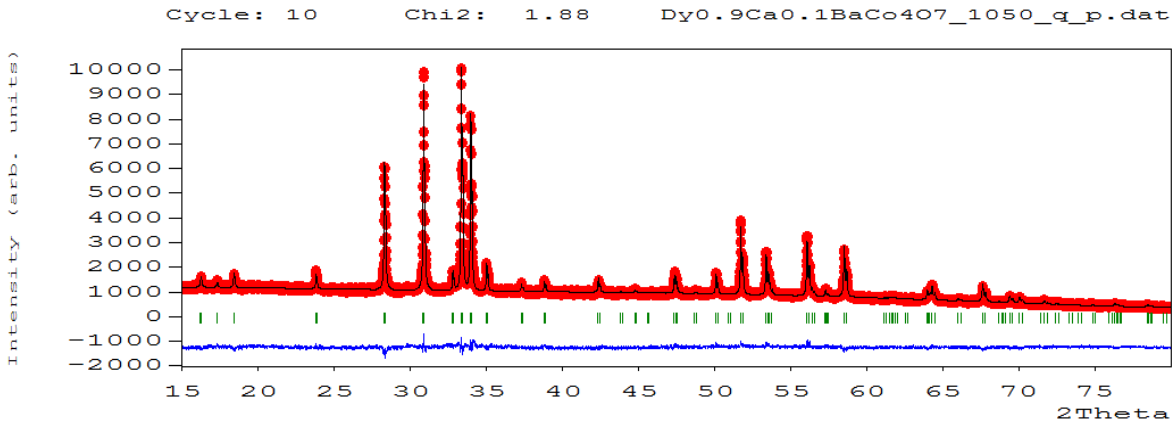

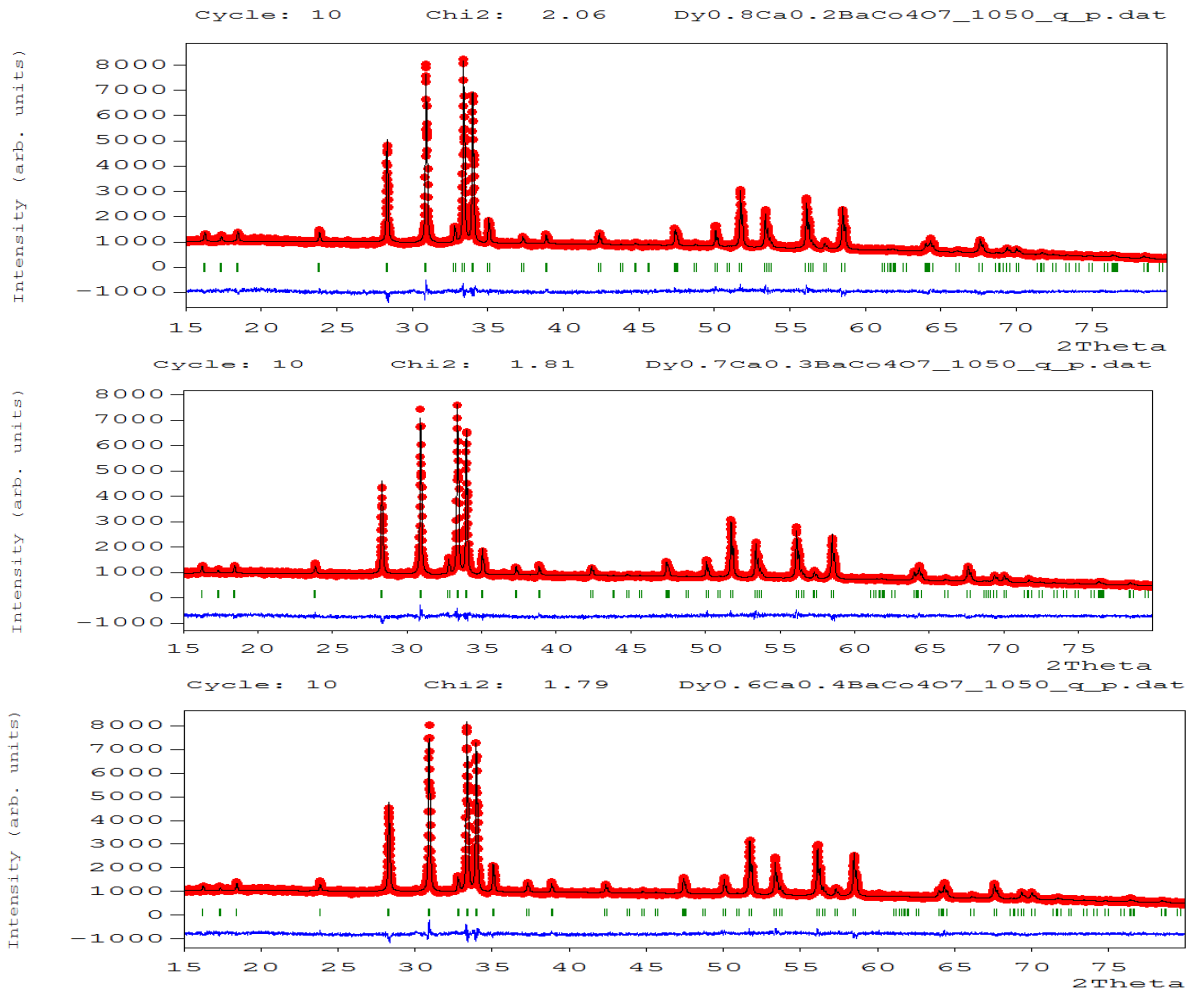

Fig 3.5) (a), (b), (c), (d) represents Rietveld Refinement for samples $Dy_xCa_{(1-x)}BaCo_4O_7$ with x = 0.9, 0.8, 0.7,0.6 respectively.

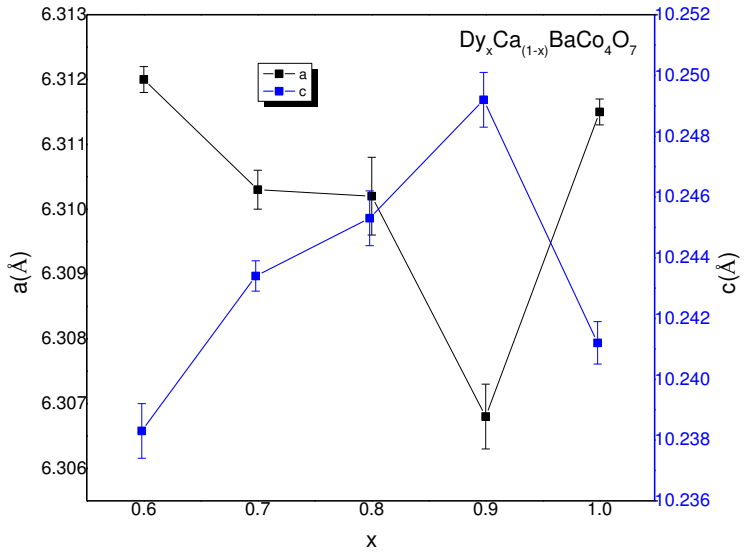

Fig. 3.6) represents the variation of lattice parameters as a function of x for samples having hexagonal P63mc space group (x = 0.6 to 1)

3.1.3) The influence of quenching in the structure of $DyBaCo_4O_7$

In this project two samples with chemical formulae $DyBaCo_4O_7$ were prepared using the synthesis method presented in section 2.1. Though the heat treatments were same for both the samples; the process of quenching at the end of the final treatment was different. First sample was quenched down to room temperature and other was quenched inside the ice. For the sake of clarity let's call these samples as $DyBaCo_4O_7$ (air) and $DyBaCo_4O_7$ (ice) respectively. The XRD data analysis of these 2 samples reveals that the $DyBaCo_4O_7$ (ice) has lower symmetry than *P63mc* $DyBaCo_4O_7$ (air) and its XRD pattern matches with $Dy_{0.5}Ca_{0.5}BaCa_4O_7$ (fig. 3.7) and lies in the middle of the series. A combination of the two space group cannot be ruled out at present. For the sake of uniformity only the air quenched samples are discussed in the series analysis.

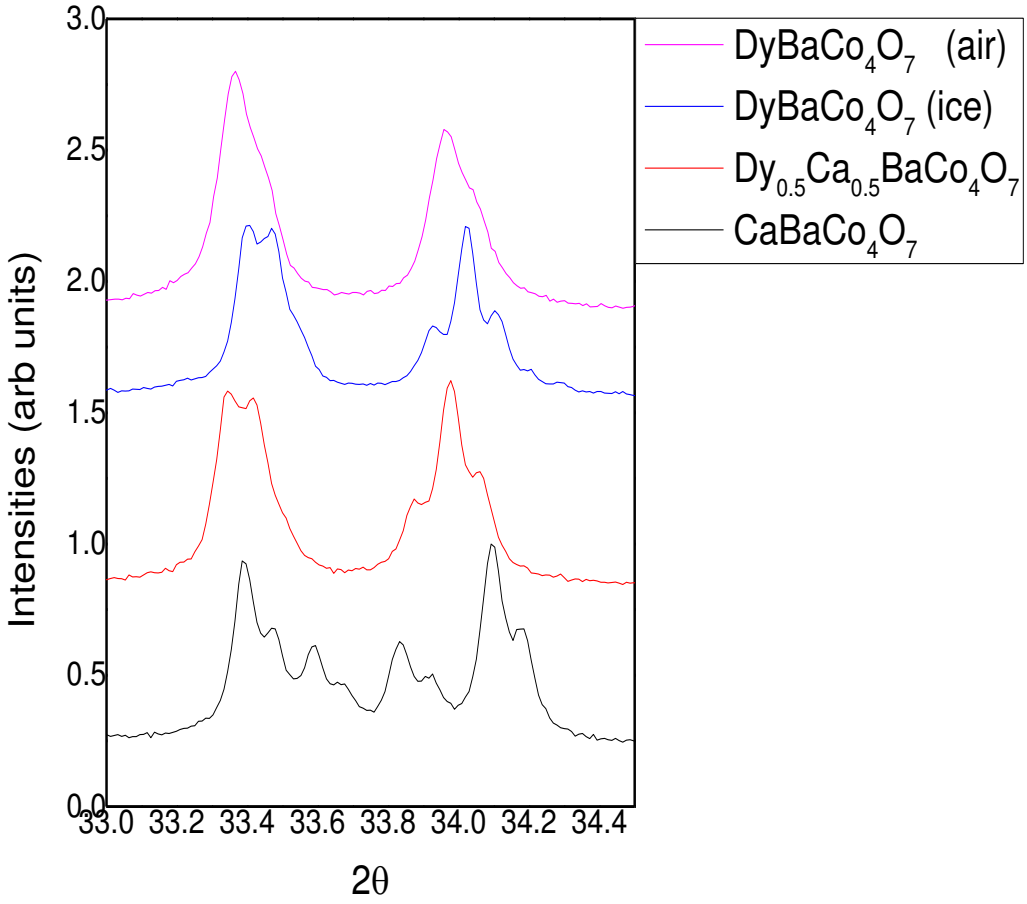

Fig. 3.7) shows the XRD patterns with pink, blue, red and black colours represent the compounds $DyBaCo_4O_7$ (air), $DyBaCo_4O_7$ (ice), $Dy_{0.5}Ca_{0.5}BaCo_4O_7$ and $CaBaCo_4O_7$ respectively expanded in the region of 2θ *range of 33° to 34.5°.*

3.2) Magnetic and Dielectric Properties

3.2.1) $CaBaCo_4O_7$

The Zero field cooled (ZFC) and field cooled FC measurements for $CaBaCo_4O_7$ were performed at 1 KOe for the temperature range of 2K-300K. The plot is shown in the figure 3.8. The ZFC-FC curves for $CaBaCo_4O_7$ shows the onset of ferrimagnetic transition at 70 K which agrees with the previous reports [41], [44]. Further, from dM/dT vs T (fig. 3.8 inset) curve we found $T_c \approx 58K$ which is only marginally smaller than the reported $T_c \approx 60K$. This can be possibly attributed to the different oxygen stoichiometry of our $CaBaCo_4O_7$ sample. Isothermal magnetisation measurements were performed at 2K and 300K. At 2K (fig. 3.9 (a)) a hysteresis is observed with a large coercive field of $H_c \approx 2T$ and a saturation magnetisation $M_s \approx 1\mu_b$/f.u. The spin only magnetic moment for Co^{2+} ($e_2^4t_2^3$) = 3.87 μ_b and for Co^{3+} = 4.89 μ_b and 2.44 μ_b for high ($e_2^4t_2^2$) and low ($e_2^3t_2^3$) spin states respectively. In a per formulae unit of $CaBaCo_4O_7$, $2Co^{2+}$ and $2Co^{3+}$ ions are present. For a ferromagnetically aligned Co ions in $CaBaCo_4O_7$ will give us a magnetic moment of the ≈ 10 to $14\mu_b$/f.u. Thus, the value of $M_s \approx 1\mu_b$/f.u. also corroborates the ferrimagnetic ground state of $CaBaCo_4O_7$. A sudden jump in the magnetisation measurement is observed at H = ± 2.25T, suggesting a metamagnetic transition. The MH isotherms at 300K (fig. 3.9 (b)) shows a typical paramagnetic nature is observed as a straight line.

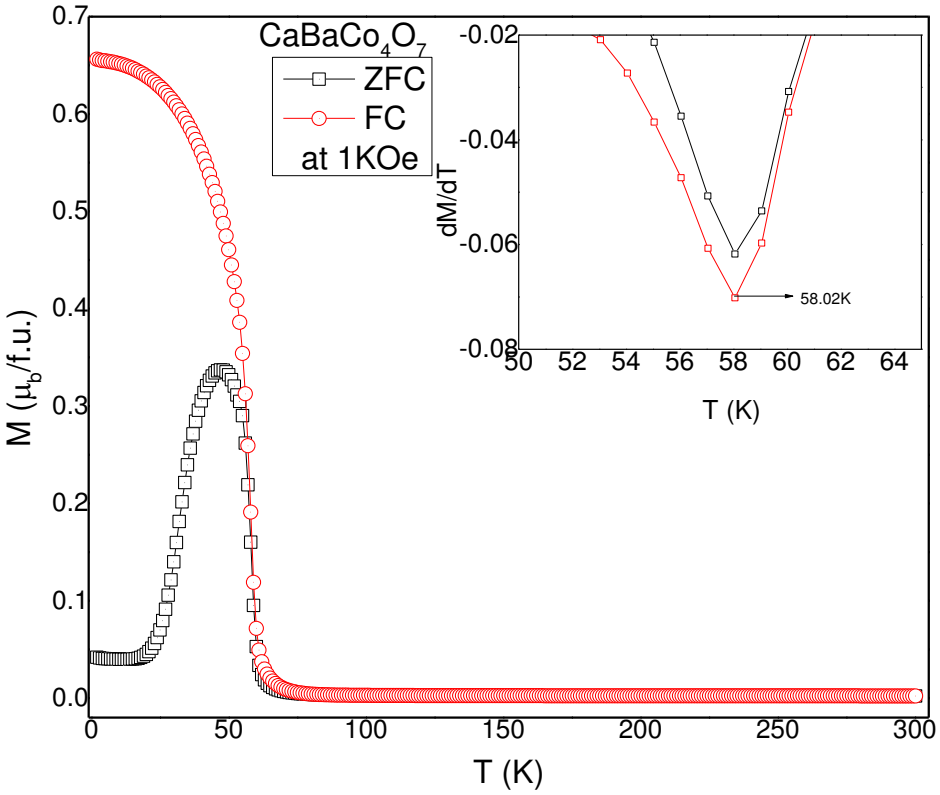

Fig. 3.8) represents ZFC – FC, M vs T curves at 1 KOe for $CaBaCo_4O_7$. In the inset dM/dT vs T is plotted with a minima at T_c = 58.02K.

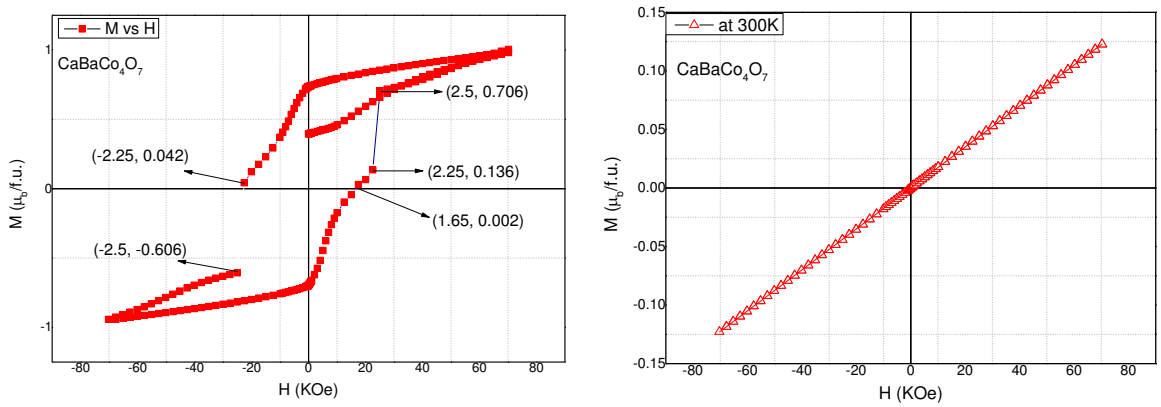

Fig. 3.9) (a) and (b) represents M vs H curves for $CaBaCo_4O_7$ at 2K and 300K respectively.

3.2.2) $DyBaCo_4O_7$

The ZFC and FC measurements for $DyBaCo_4O_7$ (air) were performed at 1 KOe for the temperature range of 2K-300K with a sweeping rate of 1K. The plot is shown in the figure 3.10. A magnetic transition in a form of a *cusp* in both ZFC-FC curves starting at $T_{cusp} \approx 80K$. The bifurcation between FC-ZFC curves starts from $T_{cusp} \approx 80K$ and it prevails down to 2K. The huge paramagnetic contribution of Dy^{3+} ion obscures the clear nature of magnetic transition and for a better manifestation paramagnetic contribution of Dy^{3+} ion is subtracted (fig. 3.11). The contribution of Dy^{3+} is calculated using the equation 3.1 [69]

$$M = NJg\mu_b B(J, x) \qquad (3.1)$$

Here, $x = Jg\mu_b H/K_b T$

M is the magnetic moment from N Dy^{3+} ions,

J = L+S = 7.5, for Dy^{3+} ($4f^9 5s^2 p^6$), S = 2.5 and L = 5,

k represents the Boltzman constant,

$$g = 1 + \frac{J(J+1) + S(S+1) - L(L+1)}{J(J+1)} = 1.38 \text{ and}$$

$B(J,x) = [(1+1/(2J)\coth(1+1/(2J)y] - 1/(2J)\coth(y/(2J)$ is the Brillioun function

Since $DyBaCo_4O_7$ has one Dy^{3+} ion per f.u, N = 1. This type of behaviour is similar to the spin glass. Above T_{cusp} there is no noticeable bifurcation between ZFC-FC curves and system behave like a paramagnetic state.

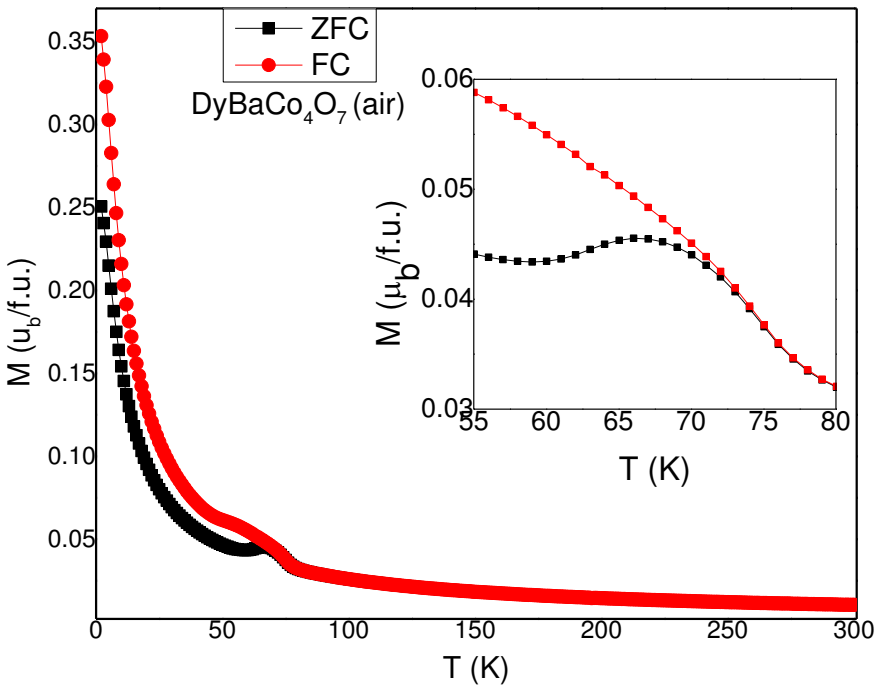

Fig 3.10) ZFC-FC magnetisation curve for $DyBaCo_4O_7$ (air) measured at field of 1 KOe. In the inset the region representing the cusp is expanded.

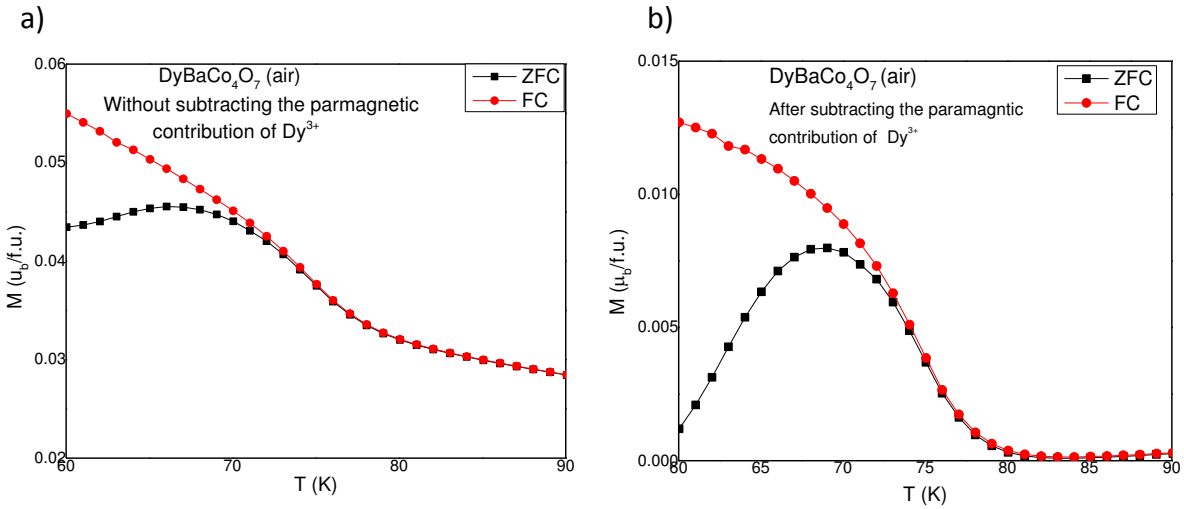

Fig 3.11) (a) and (b) represents the ZFC-FC curves for $DyBaCo_4O_7$ before and after the subtraction of the paramagnetic contribution of the Dy^{3+} ion respectively.

For $DyBaCo_4O_7$ (ice), ZFC-FC measurements were similar to $DyBaCo_4O_7$ (air), for the comparison of the magnetisation data between them, we performed the ZFC-FC measurements at fields 100 and 1K Oe. From the DC magnetisation measurements it is clear that for the spin glass like transition represented by a cusp is much more prominent in the $DyBaCo_4O_7$ (air) than $DyBaCo_4O_7$ (ice) (fig. 3.12). As mentioned earlier, these two specimens crystallize in different space group.

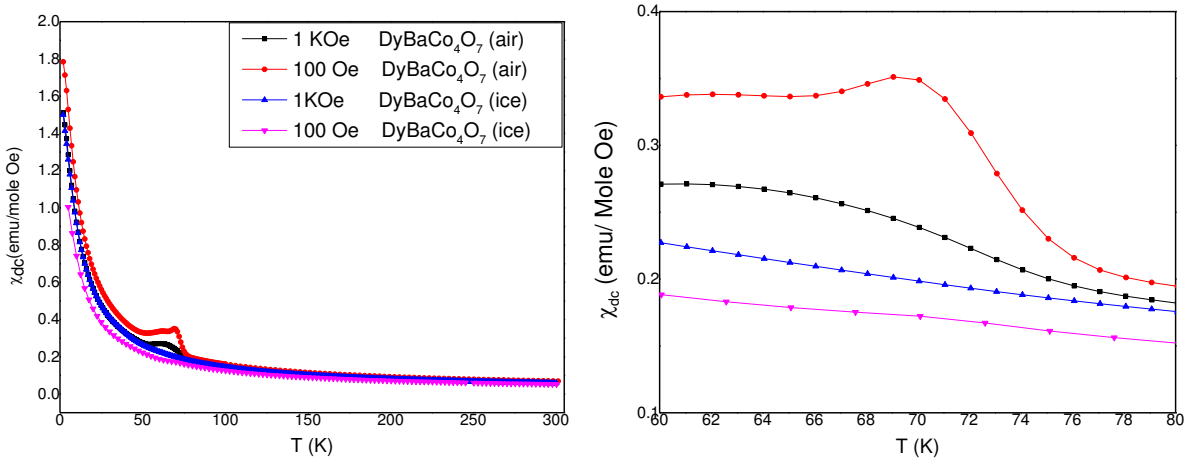

Fig. 3.12) (a) shows the ZFC curves for the samples $DyBaCo_4O_7$ (air) and $DyBaCo_4O_7$ (ice) at 100 Oe (red, pink) and at 1 KOe (black, blue), (b) represents the region near spin glass like transition (T_{cusp} ≈ 80K).

The isothermal magnetisation measurements of $DyBaCo_4O_7$ (air) at 2K and 300K are shown in the figure 3.13. At 2K, M vs H curve shows a very small hysteresis and non-saturating nature of magnetisation at an applied field of 7T. This supports the possible spin glass behaviour of $DyBaCo_4O_7$. At 300K the M vs H curve is a straight line similar to $CaBaCo_4O_7$ and represents a paramagnetic state.

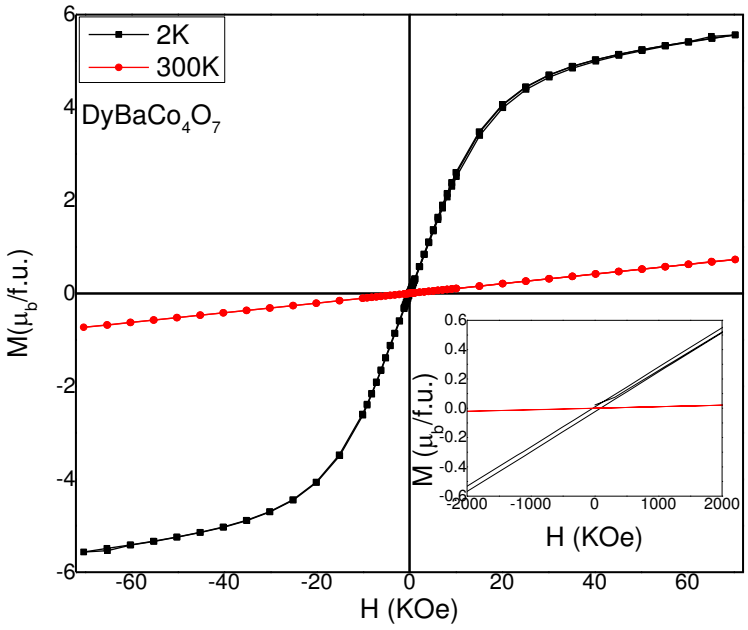

Fig. 3.13) M vs H curves for $DyBaCo_4O_7$ (air) at 2K and 300K. The inset shows a very small hysteresis near the origin (H = 0).

The dielectric measurements (e' and tanδ) for $DyBaCo_4O_7$ (air) is shown in the fig. 3.14. In the e' measurements no sharp transition or peak was found in the temperature range of 20K to 80K. For both e' and tanδ a peak like feature appears at T ≈ 47K for 10KHz frequency.

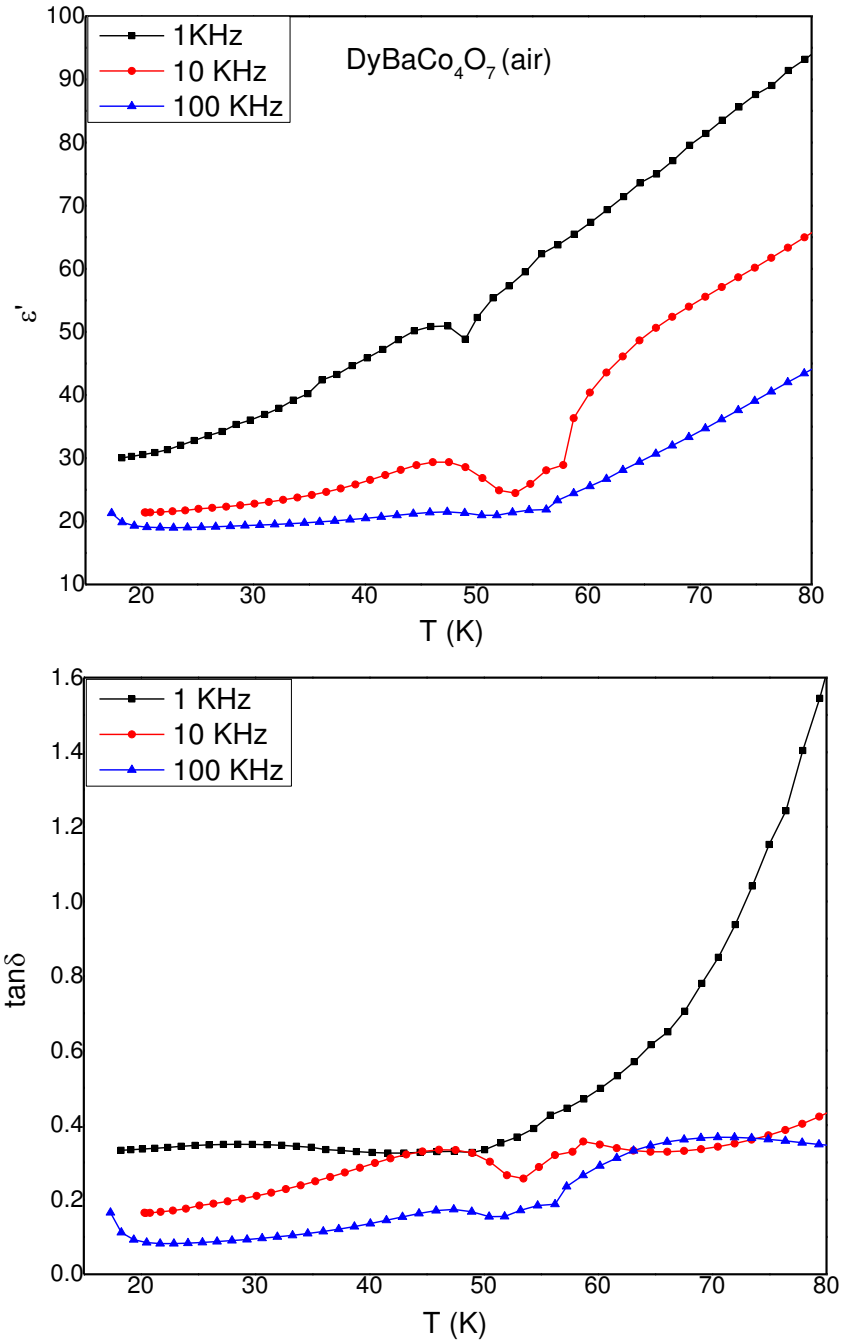

Fig 3.14) (a) and (b) graphs shows the dielectric measurements (e' vs T and tanδ vs T) of $DyBaCo_4O_7$ (air) measurements of measured at frequencies of 1KHz, 10KHz and 100KHz for the temperature range of 20K to 80K respectively.

3.2.3 *The series $Dy_xCa_{(1-x)}BaCo_4O_7$*

In this series all the samples are quenched in air. ZFC – FC measurements for the series $Dy_xCa_{(1-x)}BaCo_4O_7$ at an applied field of 1 KOe are shown in the figure 3.15. The parent compounds of the series are $CaBaCo_4O_7$ and $DyBaCo_4O_7$ and have already been discussed before. A non-overlapping nature of ZFC and FC is observed near temperature 2K for the compounds with x = 0.1, 0.6, 0.7, 0.8 and 0.9 (fig 3.15 b). Finding the onset temperature of the ZFC-FC splitting in these compounds is difficult due to the very small splitting but it is clear from the fig. 3.15 c that they are in between 40 to 80K. For the compounds with x = 0.2, 0.3, 0.4 and 0.5, no ZFC-FC splitting was observed throughout the temperature range of 2K to 300K.
For all the compound, ZFC χ_{dc} vs T data in the range for the temperature range of 200K – 300K (fig. 3.16) is fitted using the Curie-Weiss law [$\chi = \chi_0 + C/(T - T_c)$], here χ, χ_0, C and T_c represents magnetic susceptibility, temperature independent susceptibility, Curie constant and Curie temperature respectively. The derived constants are shown in the table 3.2. Using Curie constant (C), μ_{eff} per f.u. is calculated using the equation 3.2.

$$(\mu_{eff})^2 = 3Ck/N\mu_b^2 = (\mu_{eff}(Dy^{3+}))^2 + (\mu_{eff}(Co^{2+} \text{ and } Co^{3+}))^2 \qquad (3.2)$$

here, C is curie constant in emu K / mole Oe,
k represents the Boltzman constant (1.38×10^{-16} erg/K),
N is Avogadro number (6.022×10^{23}),
μ_b stands for Bohr magneton (9.274×10^{-24} J/T)

To get the average contribution of Co ions per f.u. the paramagnetic contribution of Dy^{3+} = $10.6\mu_b$ per f.u. is subtracted. The magnetic contribution of Dy^{3+} is calculated using the equation 3.1. It is clear from the graph (fig. 3.16) that $CaBaCo_4O_7$ does not follow a Curie Weiss law in the temperature range 200 to 300K. This result also agrees with the report by *Zhe Qu* [44], in this report they measured the χ up to 800K and showed that the $1/\chi$ deviates from the Curie Weiss behaviour near T ≈ 360K. Except for $CaBaCo_4O_7$, all the curves shows a reasonable Curie-Weiss fit in the temperature range of 200K – 300K but as temperature decreases all the curves starts deviating from this behaviour at around T ≈ 150K, also for all these compounds ($0.1 \leq x \leq 1$) the T_c is negative, indicating antiferromagnetic interactions.
Theoretically we can calculate the spin only contribution of Co^{2+} and Co^{3+} ions per f.u. for the compounds $Dy_xCa_{(1-x)}BaCo_4O_7$ using the equation 3.3

$$(\mu_{eff}(aCo^{2+}, bCo^{3+}))^2 = ag^2(S_{Co^{2+}}(S_{Co^{2+}}+1))^2 + bg^2(S_{Co^{3+}}(S_{Co^{3+}}+1))^2 \qquad (3.3)$$

For spin only moment g = 2. Here a and b are the number of Co^{2+} and Co^{3+} ions present in 1 f.u. of $Dy_xCa_{(1-x)}BaCo_4O_7$. In $Dy_xCa_{(1-x)}BaCo_4O_7$ Dy^{3+}, Ca^{2+} and O^{2-} and a + b = 4. The Co^{2+} will have

S_{Co}^{2+} = 3/2 Co^{3+} and Co^{2+}can have S_{Co}^{3+} = 1 and 2 in its low high spin configurations respectively. Using these facts the ($\mu_{eff}(aCo^{2+},bCo^{3+})$) is calculated for all the possible configurations of S_{Co}^{2+} and S_{Co}^{3+} and are tabulated in the table 3.3.

Table 3.2			
Compound	Observed μ_{eff}/f.u. (μ_b)	Calculated μ_{eff} (Dy^{3+})/f.u (μ_b)(Theoretical)	μ_{eff}(Co^{2+} and Co^{3+})/ f.u.(exp)
$CaBaCo_4O_7$	12.22	0	12.22
$Dy_{0.1}Ca_{0.9}BaCo_4O_7$	4.75	1.06	4.63
$Dy_{0.2}Ca_{0.1}BaCo_4O_7$	5.55	2.12	5.13
$Dy_{0.3}Ca_{0.7}BaCo_4O_7$	6.72	3.18	5.92
$Dy_{0.4}Ca_{0.6}BaCo_4O_7$	7.53	4.24	6.22
$Dy_{0.5}Ca_{0.5}BaCo_4O_7$	8.13	5.30	6.17
$Dy_{0.6}Ca_{0.4}BaCo_4O_7$	8.88	6.36	6.20
$Dy_{0.7}Ca_{0.3}BaCo_4O_7$	9.67	7.42	6.21
$Dy_{0.8}Ca_{0.2}BaCo_4O_7$	9.60	8.48	4.52
$Dy_{0.9}Ca_{0.1}BaCo_4O_7$	10.74	9.54	4.93
$DyBaCo_4O_7$	11.78	10.6	5.15

Table 3.3				
Compound			$\mu_{eff}(aCo^{2+},bCo^{3+})$/f.u calculated	
$Dy_xCa_{(1-x)}BaCo_4O_7$	a	b	S_{Co}^{2+}=3/2 S_{Co}^{3+} = 1	S_{Co}^{2+}=3/2 S_{Co}^{3+} = 2
$CaBaCo_4O_7$	2	2	6.782	8.831
$Dy_{0.1}Ca_{0.9}BaCo_4O_7$	2.1	1.9	6.833	8.780
$Dy_{0.2}Ca_{0.8}BaCo_4O_7$	2.2	1.8	6.884	8.729
$Dy_{0.3}Ca_{0.7}BaCo_4O_7$	2.3	1.7	6.935	8.677
$Dy_{0.4}Ca_{0.6}BaCo_4O_7$	2.4	1.6	6.985	8.625
$Dy_{x0.5}Ca_{0.5}BaCo_4O_7$	2.5	1.5	7.035	8.573
$Dy_{0.6}Ca_{0.4}BaCo_4O_7$	2.6	1.4	7.085	8.520
$Dy_{0.7}Ca_{0.3}BaCo_4O_7$	2.7	1.3	7.134	8.467
$Dy_{0.8}Ca_{0.2}BaCo_4O_7$	2.8	1.2	7.183	8.414
$Dy_{0.9}Ca_{0.1}BaCo_4O_7$	2.9	1.1	7.231	8.360
$DyBaCo_4O_7$	3	1	7.280	8.306

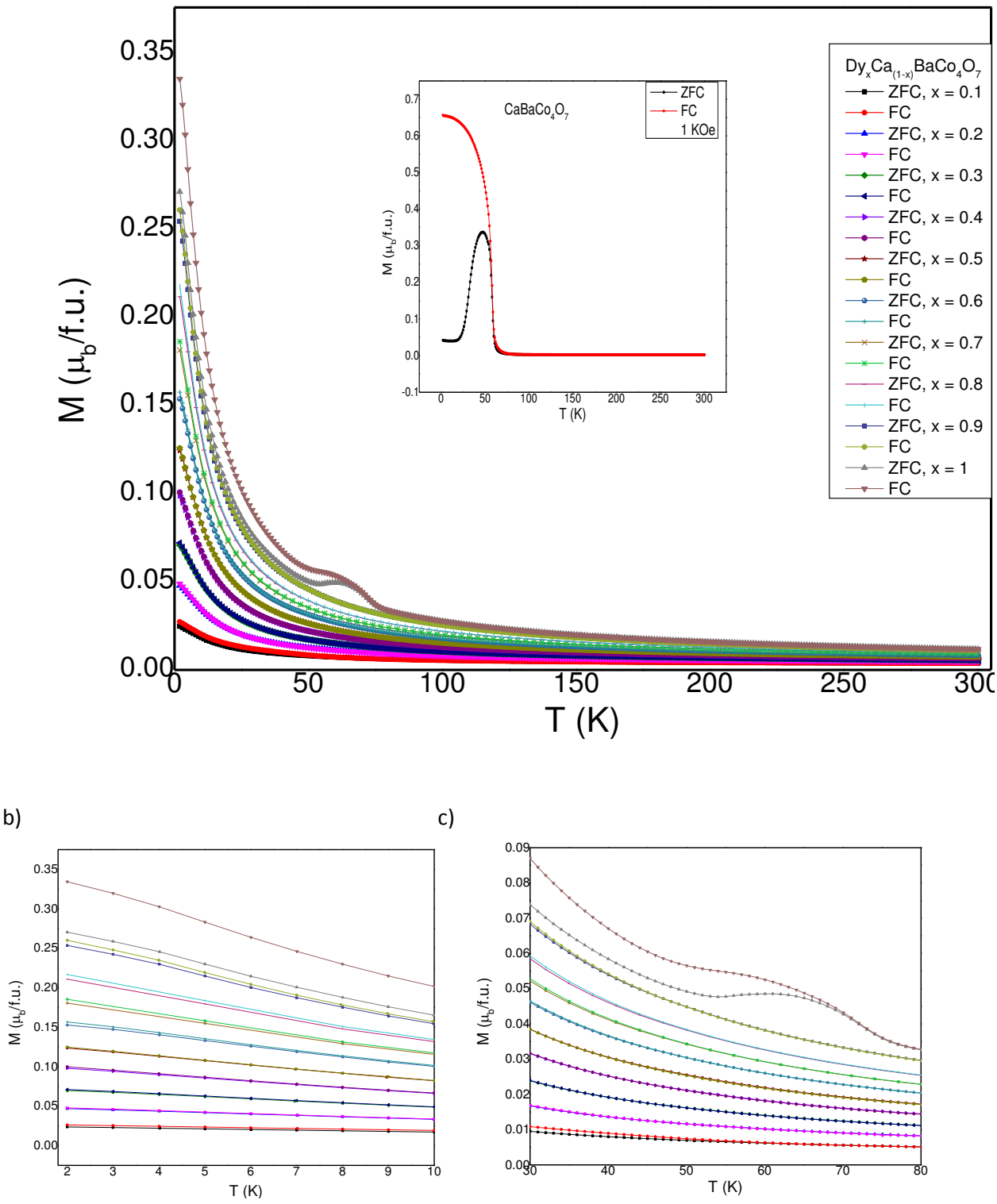

Fig. 3.15) (a) represents the ZFC – FC measurements at 1KOe, for the samples $Dy_xCa_{(1-x)}BaCo_4O_7$ for x = 0 to 1. In the inset ZFC – FC measurements are shown for $CaBaCo_4O_7$. Graphs (b) and (c) show the measurements for the temperature range of 2K to 10K and 30 to 80K respectively.

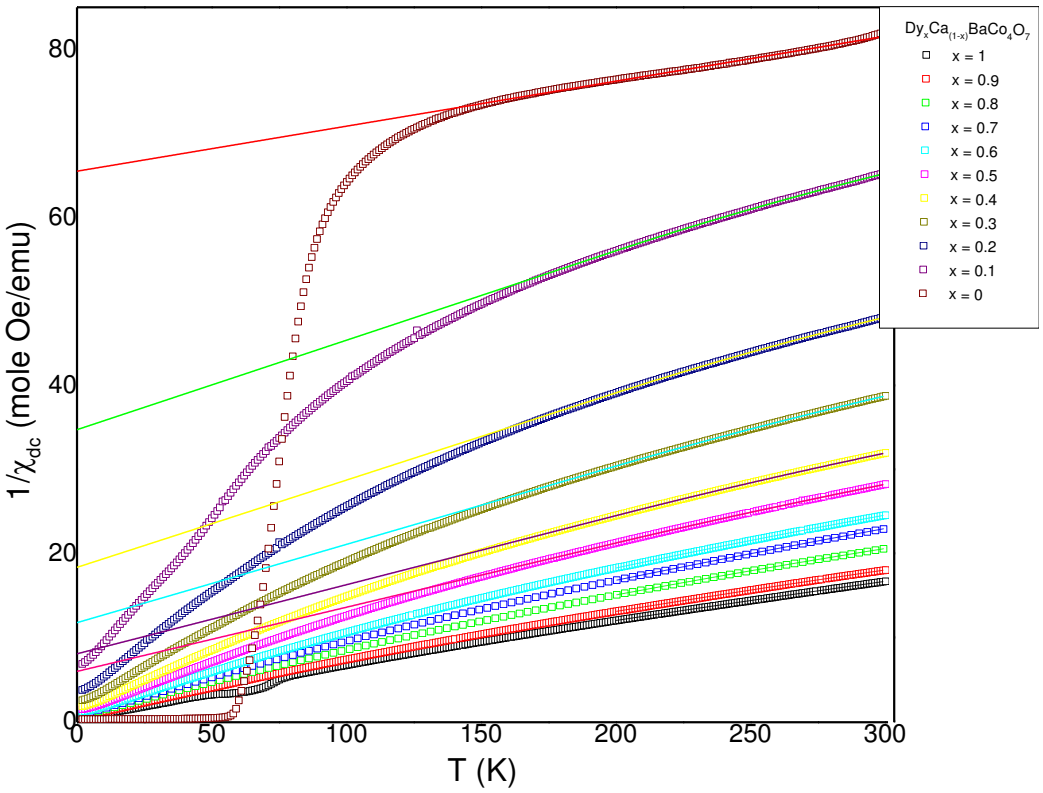

Fig. 3.16) represents the $1/\chi_{dc}$ vs T plot for the series $Dy_xCa_{(1-x)}BaCo4O_7$. The straight lines represent the Curie Weiss fit for temperature range of 200K to 300K extended in the temperature range of 2K to 300K.

The M vs H curves at 2K and 300K for the series ($Dy_xCa_{(1-x)}BaCo_4O_7$) are shown in the figure 3.17 (a) and (b). At 2K, for the samples with $0.1 \leq x \leq 1$, the maximum magnetisation (M_x) registered at H = 7T increases as x increases; a complete saturation is not achieved for any of these samples at this field. This is not surprising, since the end members have ferrimagnetic and spin glass as their low T ground state, 7T is not adequate the magnetisation in either of them. The M_x is plotted with respect to the doping level x of Dy in Ca (fig 3.18). A linear correlation between M_x and x is observed, except for the region of space group change of the series (x = 0.5 and 0.6). The nature of M_x also deviates from the linear behaviour for parent compounds $DyBaCo_4O_7$ and $CaBaCo_4O_7$. At 300K, all the samples show straight lines in the M vs H curves showing a paramagnetic nature. The slope of the straight lines increases as x increases (fig. 3.17 (b)). This could be attributed to the increasing of paramagnetic contribution of Dy^{3+} ions as x increases.

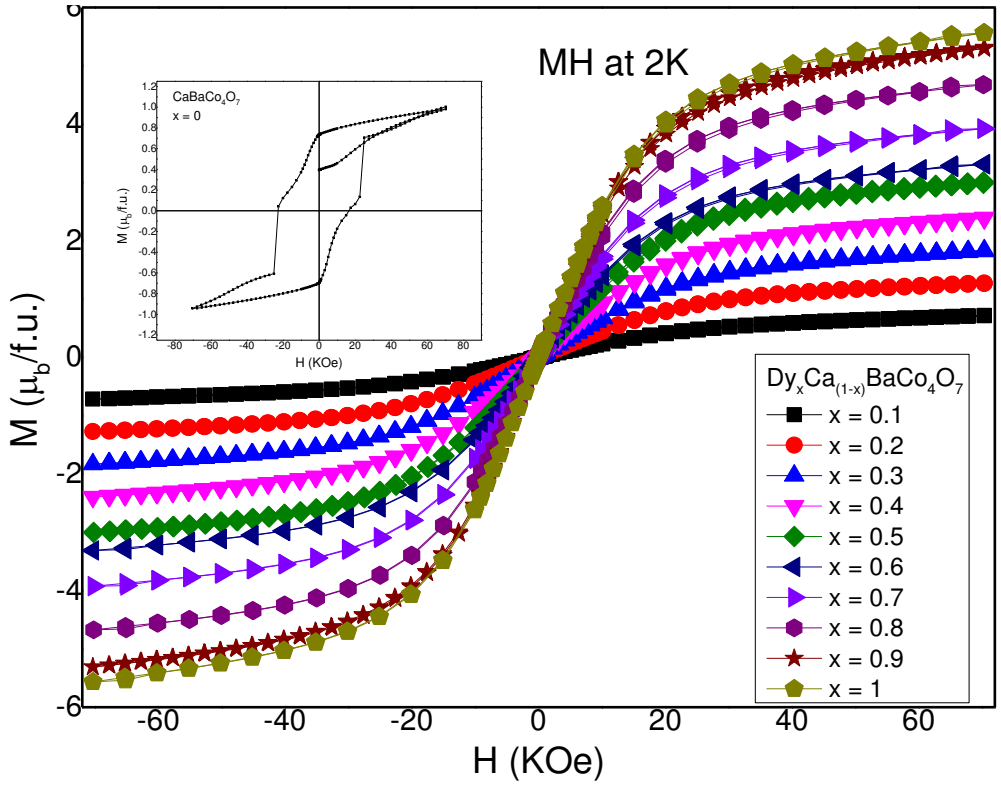

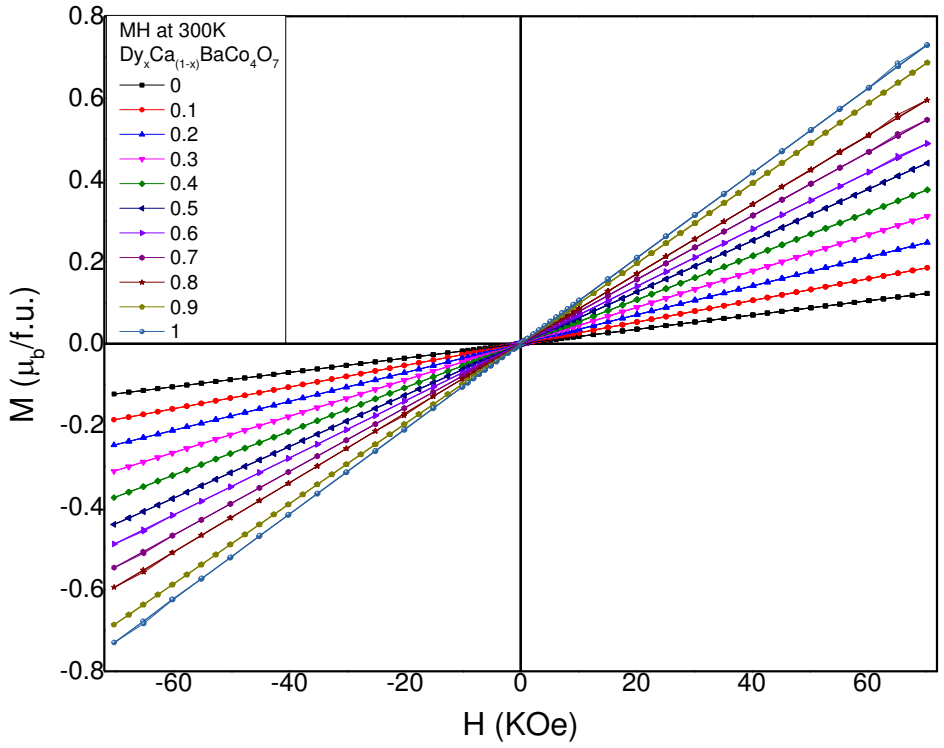

Fig. 3.17) (a) represents the M vs H curves for the series $Dy_xCa_{(1-x)}BaCo_4O_7$ at T = 2K. In the inset $CaBaCo_4O_7$ is shown separately, (b) represents the M vs H curves for the series $Dy_xCa_{(1-x)}BaCo_4O_7$ at T = 300K

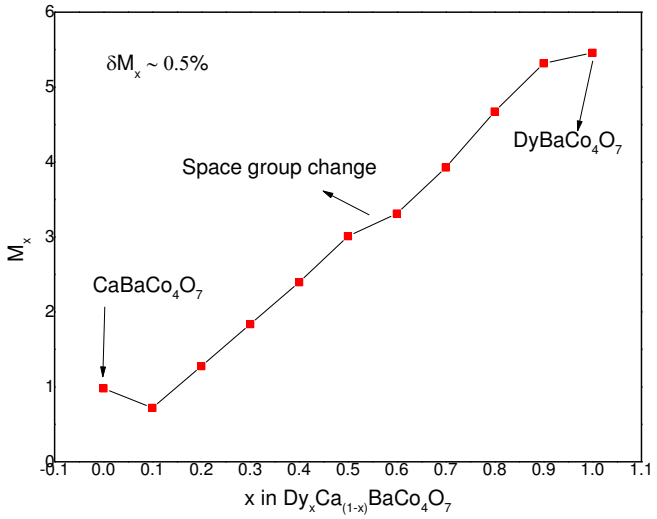

Fig. 3.18) represents the M_x (Magnetisation at 7T) vs x (x in $Dy_xCa_{(1-x)}BaCo_4O_7$)

For the analysis of magnetic interaction between Co^{2+}/Co^{3+} ions in the series, the magnetic contribution of Dy^{3+} ion is compared with the isothermal magnetisation curves at 2K (fig. 3.19). The magnetic contribution of Dy^{3+} ions per f.u. [69] is calculated using the equation 3.1. The M – M(Dy^{3+}) vs H for all the Dy containing samples are shown in fig. 3.19. For all the samples the M – M(Dy^{3+}) shows similar trend, as they initially decreases upto H ≈ 1.5T and then starts increasing. The surprising thing is M – M(Dy^{3+}) remains negative in between the H from 0T to 7T, also for a fixed value of H the M – M(Dy^{3+}) becomes more negative as the content of Dy increases. This situation is possible if the magnetic moment of Dy^{3+} ions is interacting antiferromagnetically with the overall magnetic moment of Co^{2+} and Co^{3+} ions.

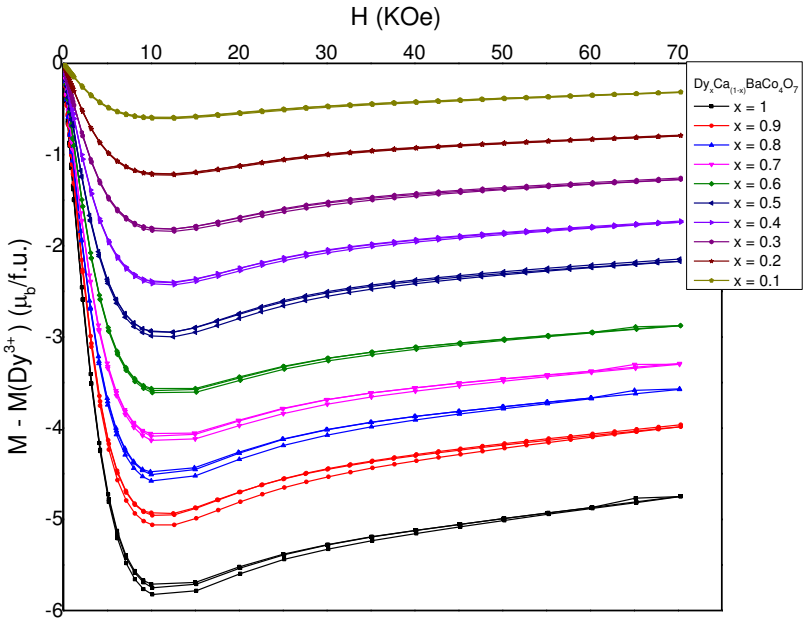

Fig 3.19) shows M – M(Dy^{3+}) vs H for the Dy containing sample at 2K.

Chapter 4: Discussions and future plans

4.1) Discussions

The results of XRD and Rietveld Refinement suggests that in the series $Dy_xCa_{(1-x)}BaCo_4O_7$, as x increases from 0 ($CaBaCo_4O_7$) to 1 ($DyBaCo_4O_7$) the structural symmetry of the compounds increases from orthorhombic *Pbn21* to hexagonal *P63mc*. The compounds with $0.6 \leq x \leq 1$, crystallises in *P63mc* symmetry. The Rietveld Refinement for the compounds with $0 \leq x \leq 0.5$ was performed using the space group *Pbn21*, but except for x = 0 ($CaBaCo_4O_7$) the refinement of atomic parameters was not possible. This could possibly be due to the biphasic (*Pbn21 and P63mc*) nature of some of these compounds. For the compounds with *P63mc* space group ($0.6 \leq x \leq 1$), we observed that lattice parameters a(Å) and c(Å) does not show a linear correlation but they show an inverse dependency with respect to each other as a function of x (fig. 3.6). There was a little control on quenching during the synthesis of these compounds. A possible reason for this anomalous behaviour of lattice parameters could be the off stoichiometry of the Oxygen in these samples. As described earlier, the structure of $DyBaCo_4O_7$ depends upon its quenching, but at this stage we also cannot rule out the possibility of different oxygen stoichiometry in the air and ice quenched samples.

The magnetic properties of the series $Dy_xCa_{(1-x)}BaCo_4O_7$ depends upon the structure and the content of Dy present in the compounds. A clear ferrimagnetic and spin glass transition is observed for $CaBaCo_4O_7$ and $DyBaCo_4O_7$ respectively, suggesting that the Co^{2+}:Co^{3+} ratio plays a crucial role in determining the ground state of the compounds. The doping of Dy in the series $Dy_xCa_{(1-x)}BaCo_4O_7$ suppresses the ferrimagnetic ground state of $CaBaCo_4O_7$. The magnetic measurements of $DyBaCo_4O_7$ (air and ice) suggests that the spin glass transition is suppressed due to the lowering of the symmetry. Even a small amount of Dy^{3+} ion (x = 0.1) is able to supress the ferrimagnetic ground state of $CaBaCo_4O_7$ and subsequent increase in the Dy^{3+} appears to destroy the long range magnetic ordering and stabilises a magnetically frustrated ground state in these systems. A clear cusp like feature was not observable in the ZFC – FC curves of Dy^{3+} containing compounds with $0.1 \leq x \leq 0.9$, presumably due to the large paramagnetic contribution of Dy^{3+}. In the high temperature region (200K – 300K), In $CaBaCo_4O_7$ a Curie-Weiss linear behaviour is not observed up-to 300K. Even if all the all the compounds with $0.1 \leq x \leq 1$ show a reasonably good Curie-Weiss fit for the temperatures of 200K to 300K, one cannot rule out the fact that it could be predominantly due to the presence of highly paramagnetic Dy^{3+} ions. High temperature M vs T measurements would be necessary, to clearly observe the true paramagnetic regime of the Co sublattice. This is also in line with some prior experimental results. The preliminary dielectric data shown in fig. 3.14 for $DyBaCo_4O_7$ (air) shows a frequency dependence ε' peaks. This is a typical dielectric behaviour of a relaxor. This also indicates that this system shows the possibility of a multiglass.

The MH curves at 2K show a metamagnetic transition in $CaBaCo_4O_7$, whereas, all the Dy doped samples exhibit a non-saturating, low coercivity hysteresis similar to the MH curves of a spin glass. To understand the dynamics of Co sublattice, ac measurements are necessary. From the real (χ') and imaginary (χ") parts of the ac susceptibility, one can observe the spin dynamics of

the system. For a paramagnet, $\chi'' = 0$ and thus, in our system, even if we have a huge paramagnetic contribution of Dy^{3+} ions, we can observe the nature of ordering in the Co sublattice using χ''.

4.2) Future plans

To perform the Rietveld Refinement of all the compounds in the series $Dy_xCa_{(1-x)}BaCo_4O_7$. It will allow us to understand how the structural properties vary as the function of x. In an attempt of calculating more accurate ratio of Co^{2+}:Co^{3+}, idiometric titration will be performed for all the compounds to determine the oxygen stoichiometry. A sample holder has been designed in order to perform high temperature DC- magnetisation measurements, which is currently under fabrication. At higher temperatures, the short range correlations will be minimised and we will be able to perform a more reliable Curie-Weiss analysis. The need of AC-measurements have already been discussed in previous section and to understand the spin dynamics of Co sublattice, we will perform (χ' and χ'') AC-magnetisation measurements in all the compounds. We also plan to perform dielectric (e' and tanδ) measurements for all the compounds.

Bibliography

1. H. Schmid: Multi-ferroic magnetoelectrics: Ferroelectrics **162:1** (1994) 317
2. M. Gajek, M. Bibes, S. Fusil, K. Bouzehouane, J. Fontcuberta, A. Barthélémy and A. Fert: Nature Materials **6** (2007) 296
3. W. Eerenstein, N. D. Mathur & J. F. Scott: Nature **442** (2006) 759
4. M. Fiebig: Journal of Physics D: Applied Physics **38** (2005) R123
5. D. I.Khomskii: Physics **2** (2009) 20
6. R.V.K Mangalam, N. Ray, U. V. Waghmare, A. Sundaresan, C.N.R. Rao: Solid State Communications **149** (2009) 1
7. D. I. Khomskii: Journal of Magnetism and Magnetic Materials **306** (2006) 1
8. J. B. Neaton, C. Ederer, U. V. Waghmare, N.A. Spaldin, K.M. Rabe: Physical Review B **71** (2005) 014113
9. N. Ikeda, H. Ohsumi, K. Ohwada, K. Ishii, T. Inami, K. Kakurai, Y. Murakami, K. Yoshii, S. Mori, Y. Horibe and H. Kito: Nature **436** (2005) 1136
10. J. V. Brink and D. I. Khomskii: Journal of Physics Condensed Matter **20** (2008) 434217
11. B. B.Van Aken, T. T.M. Palstra, A. Filippetti and N. A. Spaldin: Nature Materials **3** (2004) 164
12. T. Kimura: Nature **426** (2003) 55
13. M. Kenzelmann, A.B. Harris, S. Jonas, C. Broholm, J. Schefer, S. B. Kim, C.L. Zhang, S. W. Cheong, O.P. Vajk and J.W. Lynn: Physical Review Letters **95** (2005) 087206
14. G. Lawes, M. Kwnzelmann, N. Rogado, K.H. Kin, G. A. Jorge, R.J. Cava, A. Aharony, O. Entin-Wohlman, A.B. Harris, T. Yildirim, Q. Z. Huang, S. Park, C. Broholm and A.P. Ramirez: Physical Review Letters **93** (2004) 247201
15. N. Hur, S. Park, P. A. Sharma, J. S. Ahn, S. Guha and S-W. Cheong: Nature **429** (2004) 392
16. R.D. Johnson, Sunil Nair, L.C. Chapon, A. Bombardi, C. Vecchini, D. Prabhakaran, A.T. Boothroyd and P.G. Radaelli: Physical Review Letters **107** (2011) 137205
17. Y. J. Choi: Physical Review Letters **100** (2008) 047601
18. T. Kimura: The Annual Review of Material Research **37** (2007) 387
19. H. Katsura, N. Nagaosa and A. V. Balatsky: Physical Review Letters **95** (2005) 057205
20. S.W. Cheong and M. Mostovoy: Nature **6** (2007) 13
21. Hua Wu, T. Burnus, Z. Hu, C. Martin, A. Maignan, J.C. Cezar, A. Tanaka. N. B. Brookes, D.I. Khomskii and L.H. Tjeng: Physical Review Letters **102** (2009) 026404
22. C. Rabbow , Hk. Muller-Buschbaum: Z. Naturforsch **51b** (1993) 343
23. M. Valldor and M. Andersson: Solid State Science **4** (2002) 923
24. M. Valldor: Journal of Physics: Condensed Matter **16** (2004) 9209
25. M. Vallador: Solid State Sciences **6** (2004) 251
26. Inaugural Dissertation Stephan Buhrandt 2015: University of Cologne
27. S. Buhrandt and L. Fritz: Physical Review B **90** (2014) 020403
28. S. Buhrandt and L. Fritz: Physical Review B **90** (2014) 094415

29. E.V. Tripis, D.D. Khalyavin, S.V. Shiryaev, K.S. Redkina, P. Numez: Materials Chemistry and Physics **92** (2005) 33
30. M. Avdeev, V.V. Kharon, E.V. Tripsis: Journal of Solid State Chemistry **183** (2010) 2506
31. N. Nakayama, T. Mizota, Y. Ueda, A.N. Sokolov, A.N. Vasiliev: Journal of Magnetism and Magnetic Materials **300** (2006) 98
32. L.C. Chapon, P. G. Radaelli, H. Zheng and J. F. Michell: Physical Review B **74** (2006) 172401
33. M.Soda, Y. Yasui, T. Moyoshi, M.Sato, M. Igawa, K.Kakurai: Journal of Magnetism and Magnetic Materials: **310** (2007) 441
34. A. Huq, J.F.Michell, H. Zheng, L.C. Chapon, P.G. Radaelli, K.S. Knight, P.W. Stephens: Journal of Solid State Chemistry **179** (2006) 1136
35. A. Maignan, V. Caignaert, V. Pralong, D. Pelloquin, S. Hébert: Journal of Solid State Chemistry **181** (2008) 1220
36. B. Raveau, V. Caignaert, V. Pralong, D. Pelloquin and A. Maignan: Chemistry of Materials **20** (2008) 6295
37. V. Caignaert, A. M. Abakumv, D. Pelloquin, V. Pralong, A. Maignan, G. Van Tendeloo and B. Raveau: Chemistry of Materials: **21** (2009) 1116
38. M. Markina, A. M. Vasiliev, N. Nakayama, T. Mizota, Y. Yeda: Journal of Magnetism and Magnetic Materials **322** (2010) 1249
39. V. Pralong, V. Caignaert, A. Maignan and B. Raveau: Journal of Material Chemistry **19** (2009) 8335
40. D.D. Khalyavin, L.C. Chapon and P.G. Radaelli: Physical Review B **80** (2009) 144107
41. V. Caignaert, V. Pralong, A. Maignan and B. Raveau: Solid State Communication **149** (2009) 453
42. V. Caignaert, V. Pralong, V. Hardy, C. Ritter and B. Raveau: Physical Review B **81** (2010) 094417
43. Tapati Sarkar, V. Caignaert, P. Pralong and B. Raveau: Chemistry of Materials **22** (2010) 6467
44. Z. Qu, L. Ling, L. Zheng, Li Pi, Y. Zhang: Solid State Communications **151** (2011) 917
45. S. Chatterjee and T. Saha-Dasgupta: Physical Review B **84** (2011) 085116
46. M. Valldor, R. P. Hermann, J. Wuttke, M. Zamponi and W. Schweika: Physical Review B **84** (2011) 224426
47. K. Singh, V. Caignaert, L. C. Chapon, V. Pralong, B. Raveau and A. Maignan: Physical Review B: **86** (2012) 024410
48. T. Sarkar, Md. Motin Seikh, V. Pralong, V. Caignaert and B. Raveau: Applied Physics Letters **100** (2012) 232401
49. T. Sarkar, Md. Motin Seikh, V. Pralong, V. Caignaert and B. Raveau: Journal of Materials Chemistry **22** (2012) 18043
50. Md. Motin Seikh, Tapati Sarkar, V. Pralong and B. Raveau: Physical Review B **86** (2012) 184403
51. H. Iwamoto, M. Ehara, M. Akaki and H. Kuwahara: Journal of Physics: Conference Series **400** (2012) 032031

52. Md. Motin Seikh, Tapati Sarkar, V. Pralong, V. Caignaert and B. Raveau: Journal of Applied Physics **113** (2013) 053910
53. H. Hao, Q. He, Y. Cheng, L. Zhao: Journal of Physics and Chemistry of Solids **75** (2014) 495
54. V. Caignaert, A, Maignan, K.Singh, Ch. Simon, V. Pralong, B. Raveau, J.F. Mitchel, H. Zheng, A. Huq and L.C. Chapon: Physical Review B **88** (2013) 174403
55. R. D. Johnson, K. Cao, F. Giustino and P.G. Radaelli: Physical Review B **90** (2014) 045129
56. W. Wong-Ng, W. Xie, Y. Yan, G. Liu, J. Kaduk: Journal of Applied Physics **110** (2011) 113706
57. S. Avci, O. Chmaissem, H. Zheng, A. Huq, D.D. Khalyavin, P.W. Stephens, M. R. Suchomel, P. Manuel and J. F. Mitchell: Physical Review B **85** (2012) R220301
58. V. Duffort, T. Sarkar, C. R. Serrao, V. Pralong, V. Caignaert, A. Maignan, and B. Raveau: Journal of Materials Chemistry **22** (2012) 18923
59. D.D. Khalyavin, P. Manuel and L.C. Chapon: Physical Review B **85** (2012) R220401
60. B. Raveau, V. Pralong, V. Caignaert and A. Maignan: Z. Anorg. Allg. Chem. **637** (2011) 1079
61. M. Maignan, V. Caignaert, D. Pelloquin, S. Hebert and V. Pralong: Physical Review B **74** (2006) 165110
62. R. Szymczak, A.N. Bludov. S.L. Gnatchenko, S.N. Barilo, A. Jezierski and H. Szymczak: Acta Physica Polonica A **118** (2010) 2
63. Basic Solid State Chemistry, A. R. West, Wiley and sons (2012)
64. The Rietveld method, R. A. Young, Oxford University Press (2002)
65. FULLPROF Suite Programme (2.05) version July 2011
66. R. L. Falagy: Review of Scientific Instrumentations **77** (2006) 101101
67. Quantum Design MPMS SQUID: Hardware and software reference manuals
68. PhD thesis Heather Joanne Lewtas 2010: University of Oxford
69. Solid State Physics, Ashcroft and Mervin, Brooks/Cole (2011)